enanonewsletter

No. 23 /// October 2011 www.phantomsnet.net

NANOLITHOGRAPHY

NEW

Raith

INNOVATIVE SOLUTIONS FOR NANOFABRICATION AND SEMICONDUCTOR NAVIGATION

The nanopatterning benchmark for upgrading your FIB-SEM

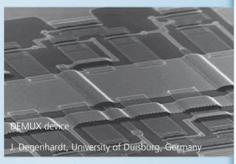

EBL

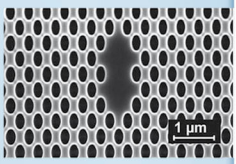

IBL

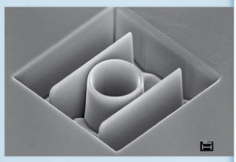

Milling

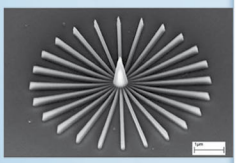

EBID

ELPHY™ *MultiBeam*

optimized for both ion & electron beam techniques

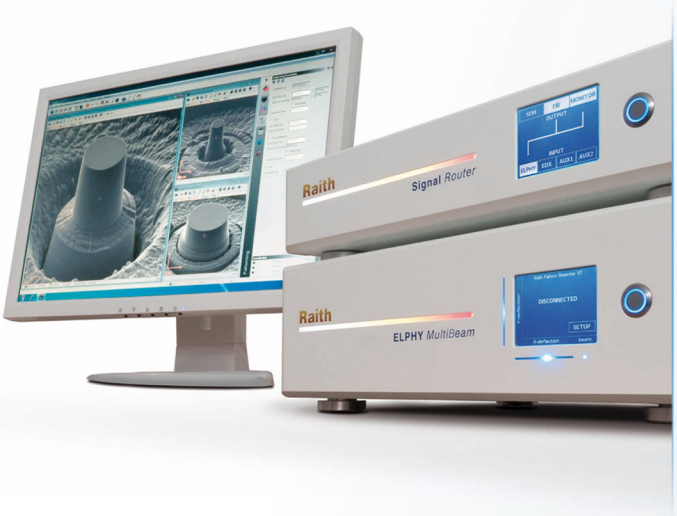

... including all comprehensive multiple technique nanopatterning functionality for

- ✓ *Focused Ion Beam Milling, Etching and Deposition*
- ✓ *Ion Beam Lithography*
- ✓ *Electron Beam Lithography*
- ✓ *Gas assisted Focused Electron and Ion Beam Induced Processing (Material Deposition / Etching)*
- ✓ *Helium Ion Beam Patterning*

contents

editorial information

No 23. October 2011. Published by Phantoms Foundation (Spain)

editor > Dr. Antonio Correia > **antonio@phantomsnet.net**

assistant editors > Carmen Chacón, Viviana Estêvão, Maite Fernández, Conchi Narros and José Luis Roldán.

1500 copies of this issue have been printed. Full color newsletter available at: **www.phantomsnet.net/Foundation/newsletter.php**

For any question please contact the editor at: **antonio@phantomsnet.net**

deadline for manuscript submission
Issue No 25: February 29, 2012.
Issue No 26: April 30, 2012.

depósito legal
legal deposit
BI-2194/2011

printing
Gráficas
Valdés, S.L.

dear readers,

During the last decades a large effort has been invested in the development of a new discipline devoted to benefit from optical excitations in materials where metals are key element (Plasmonics). We will make an introduction on this topic below, but let's anticipate that two application areas are sensing and information technologies.

In the first case, it is the strong dependence of the plasmon resonance on the environment the factor that is used for the development of applications. In the second, it is the capability to confine the electromagnetic field beyond the diffraction limit when coupling to the plasmon what is put to work. In both cases there is way for improvement, and we have identified an element that can be used in both areas, and in turn make an interesting influence in another field of research: magneto-optics. Magneto-optics is a discipline that has been tied to the information technologies framework from long ago, mainly to endorse active (tunable) capabilities. There will be an introductory section to the topic below.

Therefore the main idea behind the NANOMAGMA EU/NMP funded project is to get insight into the interplay between plasmonics and magneto-optics. The project has two main goals; the first is to prepare active magneto-plasmonic materials with tailored properties in the nanoscale and understanding the interactions of the magnetic properties with the plasmonic and optical ones, linked to electric charge oscillations. The second goal is to propose devices for applications that can benefit of this coupling. Since it is expected that the optical properties of these materials can be driven by using a magnetic field, this will allow designing and developing novel magneto-plasmonic devices. These devices will be of use in both areas mentioned above: sensing, i.e. a surface magneto-plasmon resonance (SMPR) sensor tailored on the nanoscale, and information technologies, i.e. non-reciprocal components for photonic integrated circuits based on magneto-plasmonic elements.

The following height extended abstracts, presented during the one-day NANOMAGMA Symposium (Bilbao, Spain – April 13, 2011: http://www.imaginenano.com/SCIENCE/Scienceconferences_PPM2011.php), reflects some of the latest developments on magneto-plasmonics.

In 2010 and 2011, the nanoICT project (EU/ICT/FET Coordination Action) launched two calls for exchange visits for PhD students with the following main objectives: 1. To perform joint work or to be trained in the leading European industrial and academic research institutions; 2. To enhance long-term collaborations within the ERA; 3. To generate high-skilled personnel and to facilitate technology transfer;

The first outcome report was published in the issue 22 (August 2011) and this edition contains four new articles providing insights in relevant fields for nanoICT.

We would like to thank all the authors who contributed to this issue as well as the European Commission for the financial support (projects nanoICT No. 216165 and NANOMAGMA No. FP7-214107-2).

> Dr. Antonio Correia Editor - Phantoms Foundation

Ultrafast acousto-magneto-plasmonics in hybrid metal-ferromagnet multilayer structures

Vasily Temnov, MIT Chemistry Department

77 Massachusetts Avenue, 02139 Cambridge, MA.
temnov@mit.edu

Nanostructured metal surfaces are presently used to effectively couple light to surface plasmons. This technology is also key to on-chip miniaturization of plasmonic sensors. Strong sub-wavelength confinement of optical surface plasmon fields combined with their macroscopic propagation distances exceeding tens of micrometers makes it possible to perform sophisticated nanoplasmonic experiments using conventional far-field optical microscopy in novel hybrid nanostructures. Combining these nano-optical experiments with femtosecond time-resolved spectroscopic pump-probe techniques opens the door to fundamental studies at the nano-scale and ultrafast characterization of nano-optical devices.

Here we present a new plasmonic sensor, based on a tilted slit-groove interferometer (Fig. 1) milled by a focused ion beam into a single noble metal film [1] or into a hybrid metal-ferromagnet multilayer structure [2].

Surface plasmons excited at the groove propagate towards the slit, where they interfere with incident light (Fig. 1b). Due to the tilt angle the optical transmission through the slit shows a pronounced periodic interference pattern (Fig. 1c). A small modulation of the complex surface plasmon wave vector is accumulated over a long propagation distance between the slit and the groove and results into measurable changes in the contrast and phase shift of the plasmonic interference pattern [1]. There exist different ways to modulate the wave vector of surface plasmons using multilayer structures.

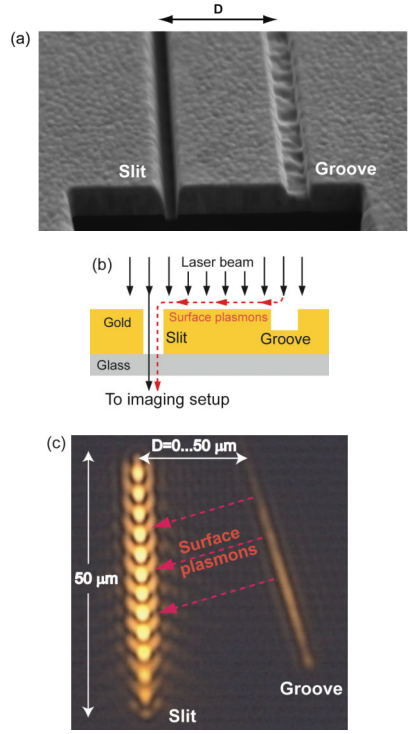

Fig. 1 > (a) Scanning electron microscopy image of a slit-groove microinterferometer in a 200 nm thin gold film. The width of the slit is 100 nm, the groove is 200 nm wide and 100nm deep. (b) The entire area of the microinterferometer is illuminated by a spatially coherent laser beam. Surface plasmon is excited at the groove, propagates towards the slit, where it is converted into free space radiation and interferes with directly transmitted light. (c) Optical transmission shows a pronounced interference pattern along the slit axis, see Ref. [1] for details./

In hybrid magneto-plasmonic gold-cobalt-gold trilayers a few nanometer thin cobalt layer is sandwiched between two gold layers

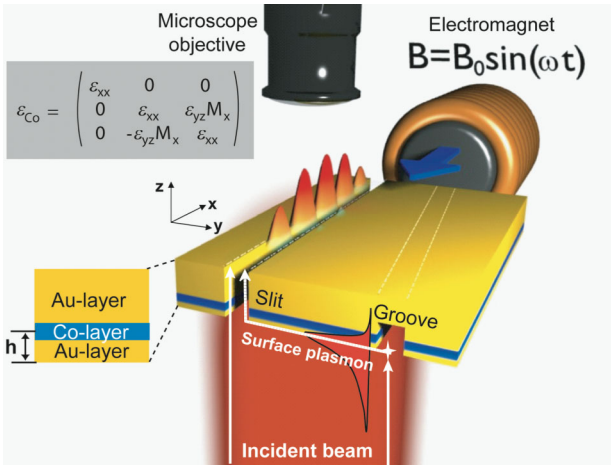

Fig. 2 > Active magneto-plasmonic interferometry in tilted slit-groove interferometers patterned in Au/Co/Au multilayer structures. The magnetic field of an electromagnet switches the magnetization in a cobalt layer and thus changes the wave vector of a surface plasmon propagating between the slit and the groove, see Ref. [2] for details./

within the skin depth of surface plasmon: $h<\delta_{skin}$=13 nm (Fig. 2). A weak external magnetic field can be used to switch the magnetization in a ferromagnetic cobalt layer and thus modify the wave vector of surface plasmons [2]. Magneto-plasmonic modulation depth of up to 2% is achieved is this geometry. It can be further increased by covering the microinterferometer with high-index dielectric material [3].

When combined with time-resolved optical pump-probe spectroscopy, femtosecond surface plasmon interferometry captures the dynamics of ultrafast electronic excitations and coherent lattice vibrations within δ_{skin}=13nm skin depth in gold with femtosecond time resolution [1]. Using a sapphire/cobalt/gold multilayer structure we generate ultrashort acoustic pulses by thermal expansion of a cobalt film impulsively heated by femtosecond laser pump pulses through the sapphire substrate (Fig. 3a). The compressive acoustic pulse propagates through the (111) gold layer at the speed of sound $c_S^{(111)}$=3450 m/s is converted into a tensile pulse upon reflection from the gold-air interface. The acoustic pulse creates a transient multilayer structure with higher (lower) density of free electrons for the compressive (tensile) acoustic pulses. The wave vector of femtosecond surface plasmon probe pulses propagating along the gold-air interface serves as a sensitive probe to the local perturbations of the electron density within the skin depth δ_{skin}=13nm induced by the acoustic pulse. Varying the pump-probe delay time makes it possible to monitor the dynamics of acoustic reflection in the plasmonic pump-probe interferogram (Fig. 3b) and extract the pump-induced modulation $\delta\varepsilon'+i\delta\varepsilon''$ of surface dielectric function ε (Fig. 3c). On top of the slowly increasing thermal background due to the temperature rise at gold-air interface the apparent acoustic echo in $\delta\varepsilon'$ is observed indicating the change of surface plasmon wave vector $\delta k_{sp}=\delta\varepsilon'/2|\varepsilon|^2$.

Straightforward mathematical analysis delivers the exponential shape of the acoustic strain pulse with the amplitude of ~10^{-3}, see Fig. 4. The exponential shape of acoustic pulses provides the heat penetration depth in cobalt within 15 nm, slightly exceeding the skin depth of optical pump pulses. A sharp sub-picosecond back front of the acoustic pulse indicates that the bandwidth of the acoustic phonons exceeds 1 THz.

The 600 fs temporal resolution in our experiment is limited by 2nm (RMS) surface roughness (SR) at gold-air interface, which acts as acoustic delay line for ultrashort acoustic pulses and prevents observation

AURIGA® 60

Information Beyond Resolution

Unique Imaging | Precise Processing | Advanced Analytics | Future Assured

Carl Zeiss MicroImaging S.L.
C / Frederic Mompou, 3
08960 Sant Just Desvern
(Barcelona)

Tel. 934 802 952
Fax 933 717 609
info@nts.zeiss.com
www.zeiss.com/nts

ZEISS

We make it visible.

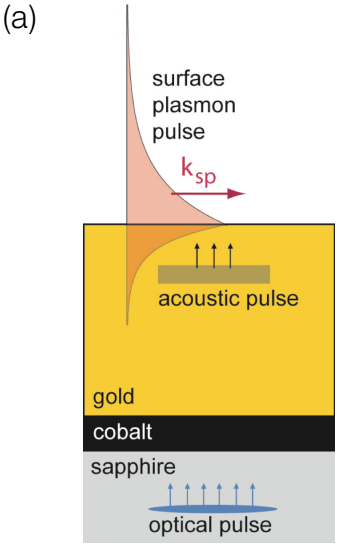

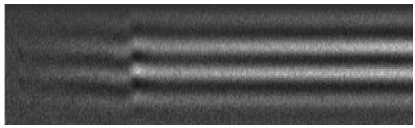

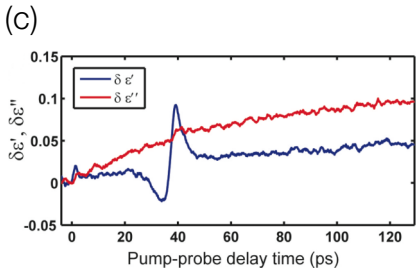

Fig. 3 > Femtosecond ultrasonics probed with ultrashort surface plasmon pulses. (a) An ultrashort compressive acoustic pulse is generated by thermal expansion of 35 nm thin fs-laser heated cobalt transducer and propagates through a 120 nm thin gold film at the speed of sound. The dynamics of acoustic reflection is captured in a plasmonic pump-probe interferogram (b) and results into the pronounced modulation of the wave vector for a time-delayed femtosecond surface plasmon probe pulse (c)./

of higher frequencies above 1 THz. A good agreement between theory and experiment is obtained by solving linear acoustic wave equation taking into account dispersion of high-frequency phonons and surface roughness. Using higher excitation fluence we were able to generate much larger acoustic pulses with strain amplitudes exceeding 1% (corresponding uniaxial strain of ~2 GPa). These giant acoustic pulses experience significant non-linear reshaping after propagation though 120 nm and 220 nm thin gold films at room temperature [4]. Numerical solutions of the Korteveg-de Vries equation provide an accurate and nearly fit-free approximation of experimental strain pulses obtained at different excitation levels. We could not observe any signatures of ultrasonic attenuation in these measurements suggesting that THz phonons in gold propagate over macroscopic distances most likely exceeding 1 micron at phonon frequency of 1 THz. Technological challenge of fabricating atomically smooth metal interfaces should be tackled in order to safely detect the acoustic phonons with frequencies exceeding 1 THz and thus provide access to the mean free path of acoustic phonons over the entire Brillouin zone. Femtosecond time-resolved pump-probe measurements in such structures may lead to the new type of acoustic spectroscopy in solids with ultrahigh (μeV) spectral resolution. Given the large amplitude, short duration and eventually loss-free propagation of acoustic pulses generated in hybrid gold-cobalt multilayer structures we envision many interesting applications for the nonlinear acoustics at the nano-scale. The possibility to switch magnetization in the magneto-plasmonic and magneto-optical devices by giant acoustic pulses represents just one example with potentially high impact in the field of ultrafast telecommunication technology.

I am indebted for the invaluable contributions to this research project by

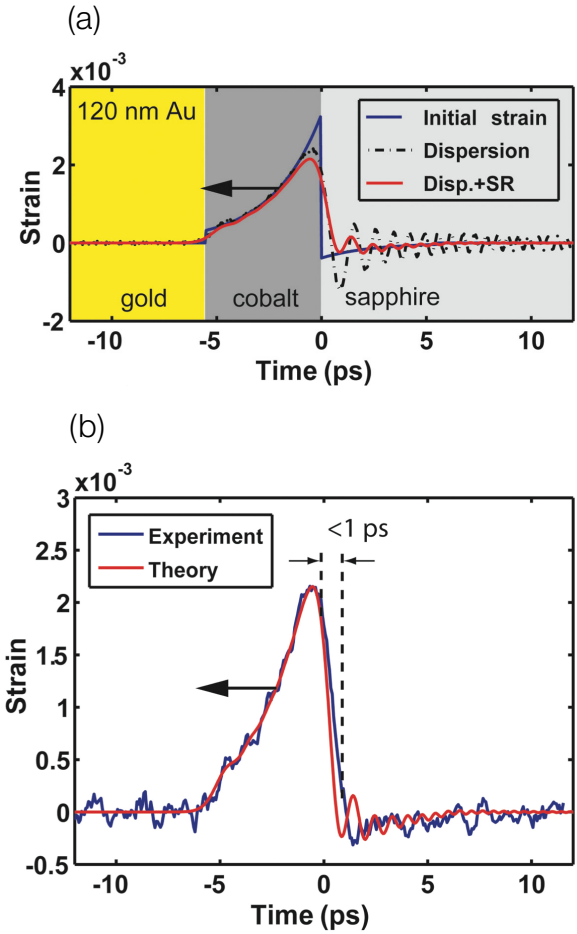

Fig. 4 > (a) The exponential acoustic pulse generated by thermal expansion of fs-laser-heated cobalt transducer is modified due to the dispersive propagation through a 120 nm thin gold layer. Surface roughness (SR) at gold-air interface smears out high-frequency components in the pulse. (b) The measured acoustic pulse (extracted from curves in Fig.3c) preserves its exponential shape and sub-picosecond acoustic front demonstrating THz bandwidth of acoustic generation. Black horizontal arrows in (a) and (b) indicate the propagation direction of the acoustic pulse, see Ref. [4] for details./

my collaboration partners from IMM-CSIC Madrid, TU Berlin, TU Chemnitz, Konstanz University and Massachusetts Institute of Technology. Financial support by the German Research Foundation and European Networks of Excellence 'Nanomagma' and 'Phoremost' is deeply appreciated.

References

[1] V.V. Temnov, K.A. Nelson, G. Armelles, A. Cebollada, T. Thomay. A. Leitenstorfer, R. Bratschitsch, Optics Express 17 (2009) 8423.

[2] V.V. Temnov, G. Armelles, U. Woggon, D. Guzatov, A. Cebollada, A. Garcia-Martin, J.M. Garcia-Martin, T. Thomay, A. Leitenstorfer, R. Bratschitsch, Nature Photonics 4 (2010) 107.

[3] D. Martin-Becerra, J.B. Gonzalez-Diaz, V.V. Temnov, A. Cebollada, G. Armelles, T. Thomay, A. Leitenstorfer, R. Bratschitsch, A. Garcia-Martin, M. Ujue-Gonzalez, Appl. Phys. Lett. 97 (2010) 183114.

[4] V.V. Temnov, C. Klieber, K.A. Nelson, T. Thomay, A. Leitenstorfer, D. Makarov, M. Albrecht, R. Bratschitsch (to be published). ✱

Label-free ligand fishing in human plasma using surface plasmon resonance and mass spectrometry imaging

Elodie Ly-Morin[1], Wilfrid Boireau[2a], Patrick Ducouroy[2b], Sophie Bellon[3], Chiraz Frydman[1]
chiraz.frydman@horiba.com

[1] HORIBA Scientific, Chilly-Mazarin, France.
[2] Clinical-Innovation / Proteomic Platform (CLIPP)
[a] Institute FEMTO-ST, Université de Franche-Comté, CNRS, ENSMM, UTBM - F, 25044 Besançon, France.
[b] Centre Hospitalier Universitaire Dijon, CGFL.
1 rue du Pr Marion, 21000 Dijon, France.
[3] GenOptics – HORIBA Scientific, Orsay, France.

We present here the exploitation of the powerful approach of Surface Plasmon Resonance imaging and Mass Spectrometry coupling for protein fishing in biological fluids such as human plasma at the same sensitivity. On one hand, multiplex format SPRi analysis allows direct visualization and thermodynamic analysis of molecular avidity, and is advantageously used for ligand-fishing of captured bio-molecules on multiple immobilized receptors on a SPRi-Biochip surface. On the other hand, MALDI mass spectrometry is a powerful tool for identification and characterization of molecules captured on specific surface. Therefore, the combination of SPRi and MS into one concerted procedure, using a unique dedicated surface, is of a great interest for functional and structural analysis at low femtomole level of bound molecules.

To reach these goals, particular surface engineering has been engaged to maintain a high level of antibody grafting and reduce non-specific adsorption. Thus, various chemistries have been tested and validated towards biological fluids such plasma, keeping in mind the capacity of the in situ investigation by MS.

Finally, signal to noise ratio was magnified leading to the characterization of protein LAG3, a potential marker of breast cancer, in human plasma.

Surface Plasmon Resonance (SPR) is an optical technique that offers label-free biomolecular analyses, providing information on kinetic processes (association and dissociation), binding affinity, analyte concentration and real time molecule detection. It has become a powerful tool for the analysis of biomolecular events involved in drug development, cancer research, and antibody screening...

The phenomenon of SPR occurs when light interacts at the interface between a biochip and a liquid medium. It permits to follow modifications of the refractive index (or the reflectivity) in real time. Such modifications are induced by a biomolecular interaction between immobilized ligands (probe molecules) and captured analytes (target molecules). SPR monitors theses changes of reflectivity to characterize the biomolecular events (such as binding and dissociation) occurring at the surface of the biochip in real time.

Surface Plasmon Resonance imaging (SPRi) technology offered by HORIBA Scientific-GenOptics takes SPR analysis a step further. The SPRi-Plex II instrument (Figure 1) enables visualizing the whole biochip surface in real-time using a video CCD camera. This design allows biochips to be prepared in an array format; with each spot corresponding to a specific immobilized ligand. Up to several hundreds different molecules can be spotted using an automated spotter, opening the way to high throughput information for biomolecular interaction. The multiplexing capabilities of SPRi can meet with any experimental design without concession. Meanwhile, the sensitivity of SPRi is not compromised as analyte concentrations can be detected down to the nanomolar range.

Fig. 1 > SPRi-PlexII system

The applications of SPRi are vast and include for example protein:protein [1], DNA:DNA [2,3], peptide:protein [4], polysaccharides:proteins [5] or protein:cells [6,7] interactions. The flexibility of the HORIBA Scientific-GenOptics instruments enables complex samples such as serum and plasma to be analyzed for clinical applications.

The coupling of SPRi biosensors and matrix-assisted laser desorption ionization mass spectrometry (MALDI-MS) is an innovative approach for biomarker discovery in biological fluids. It permits analytes captured by SPRi to be identified and characterized by their molecular weight and peptide sequence. SPRi-MS opens a new method of detection, quantification and structural characterization of proteins of interest. In the future, it could help better discriminate between sub-species within a family of biomarkers.

In this context, the complexity lies in the coupling of both techniques [8]. Most strategies require the elution of the bound analyte and its analysis by ESI- (electrospay ionisation) or MALDI-MS. This procedure has many drawbacks (analysis time, no multiplexing capabilities, decreased sensitivity, additional cross-contamination risks, etc.) which delayed the development of SPR-MS in the diagnostic field.

The open format of the HORIBA Scientific-GenOptics instruments makes MS coupling easier and faster. The possibility of direct MS analysis on the SPRi sensor was recently shown [9]. The SuPRa-MS platform (Surface Plasmon Resonance in arrays coupled with Mass Spectrometry) combines SPRi and MS in a single biochip. The biochip used for SPRi (SPRi-Slide) is directly transferred to the MS instrument. There is no need to neither elute nor re-deposit the bound analyte. The MS enzymatic digestion and the deposition of the MALDI matrix are performed directly on the SPRi-Slide. The latter is then directly placed on the MS plate holder (Figure 2).

A proof-of-concept study of SPRi-MS imaging coupling was performed for the detection of LAG3 recombinant protein in plasma. The solution fraction of this protein is a potential biomarker for breast cancer [10]. For this purpose, a mouse antibody (IgG2A) directed against LAG3 was immobilized on a SPRi-Slide using a dedicated surface chemistry compatible with MS analysis (NHS chemistry). Before injecting LAG3, rat serum albumin (RSA) was used to avoid non-specific binding on the surface of the biochip. Then, the specific interaction of LAG3 (added in plasma) and IgG2A was monitored using SPRi and images of the interaction were studied. Several femtomoles/mm^2 of LAG3

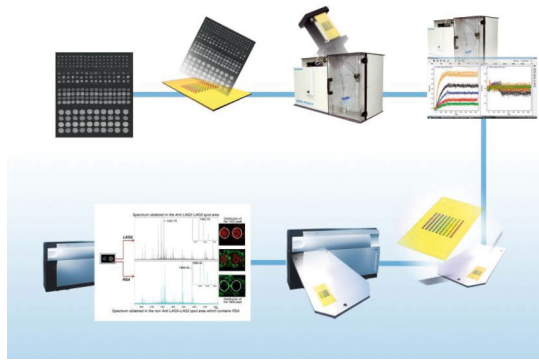

Fig. 2 > The SuPRa-MS platform

proteins were captured by SPRi. After direct processing on the biochip surface (enzymatic digestion and matrix deposition), the SPRi-Slide was analyzed using a MALDI-MS imager (Ultraflex, Bruker Daltonics). By showing the distribution of MS peaks specific of LAG3 and RSA respectively, it was possible to build the MS image of LAG3 spots (Figure 3) directly on the SPRi-Slide.

The SuPRa-MS platform pioneers the combination of SPR imaging and MS imaging (MSi). It offers the possibility to gain spatially resolved information on the capture, sequence and molecular weight of clinical biomarkers.

Multiplexed SPRi analysis using the HORIBA Scientific-GenOptics instruments provides rapid and high-throughput information in real time from up to several hundreds interactions in parallel. The technology is sensitive and does not require the use of labels. It can speed-up

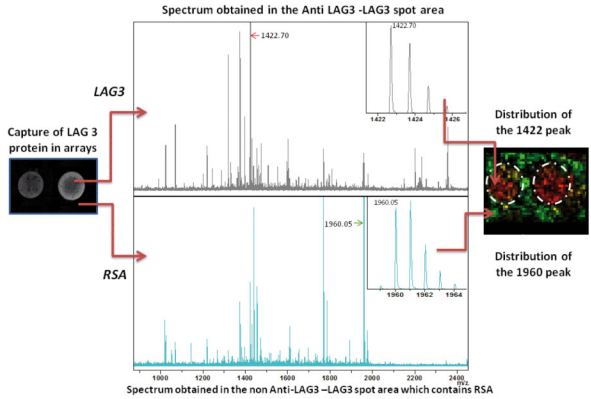

Fig. 3 > On-a-chip detection, identification and imaging of LAG3 protein (potential marker of breast cancer) at 10nM in human plasma through the SuPRa-MS platform

the workflow and reduce consumable costs during optimization processes. The coupling with MS analysis is straightforward and easier, which makes it a valuable tool for biomarker identification.

References

[1] Uzun and al. (2009) Production of surface plasmon resonance based assay kit for hepatitis diagnosis. Biosensors and Bioelectronics. 24(9): 2878-2884.

[2] Spadavecchia and al. (2009) New cysteamine based functionalization for biochip applications. Sensors and Actuators B. 143(1):139-143.

[3] Corne and al. (2008) SPR imaging for label-free multiplexed analyses of DNA N-glycosylase interactions with damaged DNA duplexes. Analyst. 133: 1036-1045.

[4] Prieto and al. (2009) Synaptonemal complex assembly and H3K4Me3 demethylation determine DIDO3 localization in meiosis. Chromosoma. 118: 617-632.

[5] Mercey and al. (2008) Polypyrrole oligosaccharide array and surface plasmon resonance imaging for the measurement of glycosaminoglycan binding interactions. Anal. Chem. 80(9): 3476-3482.

[6] Roupioz Y. and al. (2009). "Individual Blood-Cell Capture and 2D Organization on Microarrays" Small 2009, 5, No. 13, 1493–1497.

[7] Suraniti and al. (2007) Real-time detection of lymphocytes binding on an antibody chip using SPR imaging. Lab Chip. 7: 1206-1208.

[8] Boireau and al. (2009) Revisited BIA-MS combinationb: Entire "on-a-chip" processing leading to the proteins identification at low femtomole to sub-femtomole leveks? Biosensors and Bioelectronics 24: 1121-1127.[9]
Bellon and al (2009) Hyphenation of Surface Plasmon Resonance Imaging to Matrix-Assisted Laser Desorption Ionization Mass Spectrometry by On-Chip Mass Spectrometry and Tandem Mass Spectrometry Analysis. Anal. Chem. 81: 7695–7702.

[10] Triebel and al (2006) A soluble lymphocyte activation gene-3 (sLAG-3) protein as a prognostic factor in human breast cancer expressing estrogen or progesterone receptors. Cancer Letters. 235(1):147-53.

Light localization on a gold nanodisk array probed by near-field optics

Loïc Lalouat[1], Lionel Aigouy[1], P. Prieto[2], A. Vitrey[2], J. Anguita[2], A. Cebollada[2], M.U. González[2], A. García-Martín[2]

[1] LPEM, UMR 8213 CNRS-ESPCI, Ecole Supérieure de Physique et de Chimie Industrielle, 10 rue Vauquelin, 75231 Paris cedex 5, France.
[2] IMM-Instituto de Microelectrónica de Madrid (CNM-CSIC), Isaac Newton 8, PTM, Tres Cantos, E-28760 Madrid, Spain.

Arrays of metallic nanoparticles are artificial structures that can find many applications in physics and biology. When they are illuminated by an external light source, strong evanescent fields are localized in the near-field regions of the particles. These strong local fields can be used for exciting single molecules, for performing Raman scattering, for developing biochemical sensors, or for performing nanolithography [1-4]. The knowledge of the local optical properties of these structures, like the electromagnetic field distribution, is therefore of importance for developing such applications. For instance, it is interesting to know the position and the shape of the field enhancement zones with regard to the particles, as well as their vertical localization, and the influence of the incident polarization direction. For that, theoretical simulations with finite difference time domain (FDTD), finite boundary element or Green dyadic methods are often used, but the amount of experimental data available in the literature is quite reduced. In this work, we present an experimental study of the field localization on a disk array with a scanning near-field optical microscope (SNOM). Our experiments, which are in good agreement with numerical simulations, show a strong localization of the electromagnetic field between the particles, in the direction of the incident polarization.

The experimental SNOM set-up is shown in Figure 1. In contrast to other SNOM techniques [5,6], our probe is a submicron size fluorescent particle glued at the end of a sharp tip [7]. In contact with the sample surface, it absorbs the local field at the excitation wavelength and emits light at a different one. By collecting the fluorescence as a function of the tip position on the surface, we obtain a fluorescence image which is directly related to the intensity of the electromagnetic field on the surface. The particle, which contains erbium and ytterbium ions, is excited at λ=975nm and its fluorescence is detected in the visible range at λ=550nm. Since this atypical excitation

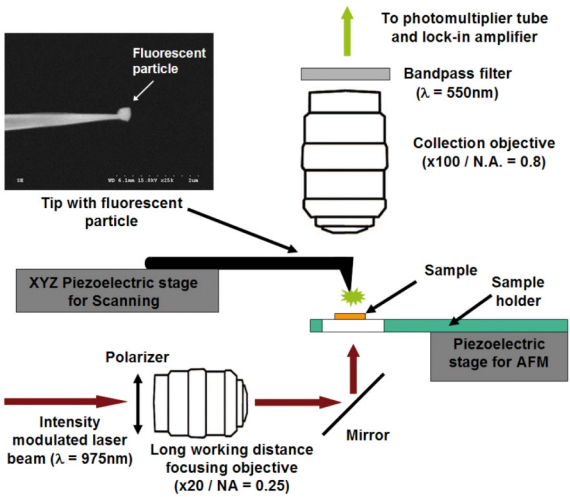

Fig. 1 > Description of the experimental set-up. The SNOM probe is a fluorescent particle glued at the end of a sharp tip.

process involves two photons, the collected fluorescence is proportional to the square of the total field intensity on the surface [7]. The sample studied is an array of gold nanodisks [diameter = 286nm, height=50nm, period=500nm, (see Figure 2)] fabricated on a glass substrate. The structure has a wide plasmon resonance peak located just below the excitation wavelength between 800 and 900nm.

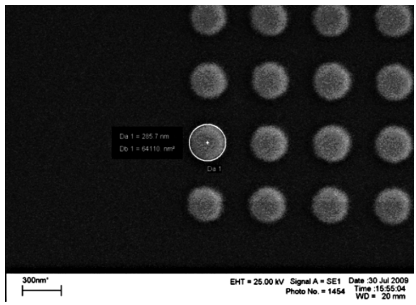

Fig. 2 > SEM picture of the studied gold nanodisk.

We show in Figure 3(a) and (b), the experimental near-field optical images of the structure measured in a non-contact mode [8]. The incident polarization is linear and indicated by the white arrow. The position of the nanodisks is represented by the dotted white circles. The images show a periodic pattern, with elongated bright spots. Each bright spot is in fact comprised of two lobes, located between the disks, and aligned in the incident polarization direction.

To check the validity of the SNOM results, we have performed an FDTD simulation of the measured signal. To make a realistic comparison, we calculated the square of the total field intensity and integrated this quantity on a volume which represents the fluorescent particle size. Such procedure only tends to broaden the size of the lobes but does not change the shape of the pattern. The simulations are represented in Figure 3(c) and (d). An excellent agreement is observed between the experimental images and the

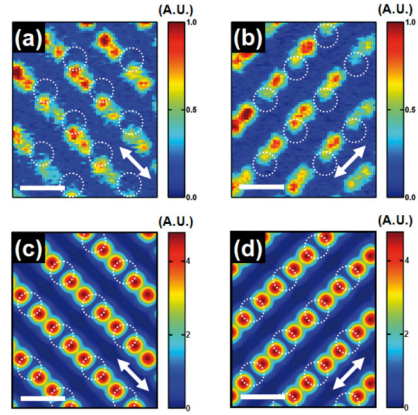

Fig. 3 > (a,b) SNOM images measured in a non-contact mode on the nanodisk array at λ=975nm. The dotted circles indicate the position of the disks. (c,d) FDTD calculations of the near-field distribution on the structures. The calculation represents the square of the intensity of the total field which is the quantity measured with the near-field fluorescent probe used in the experiments. The calculation has been performed by taking into account of the probe size (a 160 nm large cube). The white arrows indicate the incident polarization direction. The scale bar is 500 nm-long (taken from ref. 8).

theoretical ones which exhibit the same periodic pattern, and the same polarization dependence.

We show in Figure 4(a) and (b) higher resolution scans of the structure. Cross-sections extracted from the experimental and simulated images are shown in Figure 4(c) and (d). The curves are in excellent agreement in terms of relative contrast. One can clearly see that all the electromagnetic field is concentrated between the disks in the direction of the incident polarization and that almost no light is located between the disks in the direction perpendicular to the incident polarization.

Another interesting parameter which characterizes nanodisks arrays is the vertical extension of the electromagnetic field above the surface. For instance, such parameter is

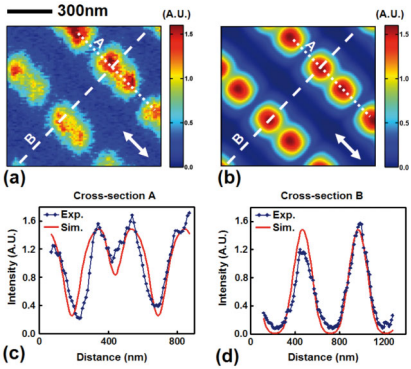

Fig. 4 > (a) : Experimental SNOM image measured on the array of gold nanodisks ; (b) FDTD simulation of the near-field optical signal; (c,d) cross-sections parallel (direction A) and perpendicular (direction B) to the incident polarization The position of the gold disks is the same than the ones shown in Fig. 3 (taken from ref. 8).

important if we want to use the structures for performing nanolithography, because it will determine the penetration depth of the light in a photoresist situated on top of the array. To have an idea of this localization, we have performed scans in planes perpendicular to the sample surface. We show in Figure 5 the experimentally measured signals which indicate that the light is essentially confined at close distance from the surface. Above 200nm, no signal is detectable anymore. Such distance depends on the structure of the array, and in particular on the disks size, their thickness and their separation.

To summarize, we have performed a study of the light localization on a gold nanodisk array by near-field optics. The near field has been measured using a fluorescent particle glued at the end of a sharp tip. The measured near-field images, which represent the square of the total field intensity, show that the light is localized between the disks in the direction of the incident polarization direction. The results are in good agreement with numerical simulations performed by finite difference time domain method.

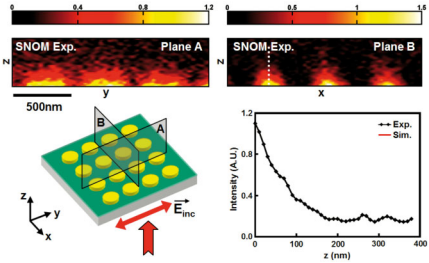

Fig. 5 > Experimental SNOM image measured in planes perpendicular to the sample surface. The scanning planes are indicated on the drawing. The curve in the bottom shows the vertical decay of the measured signal (taken from ref. 8).

References

[1] S. A. Maier, and H. A. Atwater, J. Appl. Phys. 98, 011101 (2005).

[2] N. Fang, H. Lee, C. Sun, and X. Zhang, Science 308, 534 (2005).

[3] S. S. Aćimović, M. P. Kreuzer, M. U. González, and R. Quidant, ACS Nano 3, 1231 (2009).

[4] A. F. Koenderink, J. V. Hernández, F. Robicheaux, L. D. Noordam, and A. Polman, Nano Lett. 7, 745 (2007).

[5] M. Schnell, A. Garcia-Etwarri, A. J. Huber, K. Crozier, J. Aizpurua, and R. Hillenbrand, Nat. Photon. 3, 287 (2009).

[6] M. Salerno, N. Félidj, J. R. Krenn, A. Leitner, F. R. Aussenegg, and J. C. Weeber, Phys. Rev. B 63, 165422 (2001).

[7] L. Aigouy, Y. De Wilde, and M. Mortier, Appl. Phys. Lett. 83, 147 (2003).

[8] L. Aigouy, P. Prieto, A. Vitrey, J. Anguita, A. Cebollada, M.U. González, A. García-Martín, J. Labéguerie-Egéa, M. Mortier, J. Appl. Phys. 110, 044308 (2011). ✱

Controlling fluorescence resonant energy transfer with a magneto-optical nanoantenna

R. Vincent and R. Carminati

Institut Langevin, ESPCI ParisTech, CNRS,
10 rue Vauquelin, 75231 Paris Cedex 05, France.

Energy transfer between a molecule in an excited state (donor) and a molecule in the ground state (acceptor) underlies many significant photophysical and photochemical processes, from photosynthesis to fluorescence probing of biological systems. It is also of interest in nanophotonics where efficient transfer of optical excitations on subwavelength scales is a key issue. Depending on the separation between the donor (D) and the acceptor (A), the process can be described accurately by various theories accounting for the electromagnetic interaction between the two species. For a D-A distance range on the order of 2-10 nm, which is relevant for photochemical studies and nanophotonics, the well-established Förster theory [1] based on quasi-static dipole-dipole interaction has been very successful. It shows that while Förster Resonant Energy Transfer (FRET) is a very useful process that can be used, for example, as a ruler for spectroscopic measurements [2], it is a rather weak process that goes down as the inverse sixth power R^6 of the D-A separation [3]. In fact, one can introduce a length scale known as the Förster distance R_0 at which FRET is 50% efficient and it is found that R_0 is on the order of a few nanometers in most practical situations. For even smaller distances, Dexter [4] recognized that electronic exchange and multipolar interactions become important and a full quantum mechanical treatment must be implemented. On the other hand, in the large distance regime (non-negligible compared to the wavelength), full electrodynamics is needed to account for retardation effects.

In the present work, we use an established general framework for dipole-dipole energy transfer between an emitter and an absorber in a nanostructured environment [5]. The theory allows us to address FRET between a donor and an acceptor in the presence of a nanoparticle with an anisotropic electromagnetic response. For the case of a nanoparticle with an anisotropic dielectric response (e.g., a nanoparticle made of a ferromagnetic material exhibiting a magneto-optical response), the distance dependence, the orientation dependence and the strength of the FRET efficiency can be changed substantially. In the case of a magneto-optical anisotropy, it can in principle be controlled using the static magnetic field as an external control parameter.

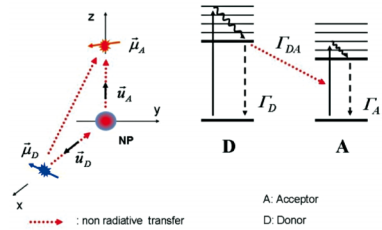

Fig. 1 > Left panel: Schematic configuration of the D-A system in the presence of a nanoparticle. The different channels for energy transfer (direct or indirect) are indicated by dotted arrows. When the transition dipoles are orthogonal, the direct Förster transfer is disabled. Right panel: Energy-level diagram of the FRET process between a donor and acceptor molecules.

In principle, the presence of a nanostructure close to a D-A couple will modify the emission and absorption by the transition dipoles; here we use the formalism to express explicitly the FRET rate of a D-A couple interacting with a spherical nanoparticle exhibiting a

purely metallic response or a magneto-optical response. We have shown previously [5], that the FRET rate mediated by the nanoparticle can be expressed simply as follows

$$\frac{\Gamma_{DA}^{NP}}{\Gamma_0} = \left[\frac{R_0}{R_A}\right]^6 \left(\frac{R_p}{R_D}\right)^6$$

In this expression Γ_{DA}^{NP} is the energy transfer rate from donor to acceptor mediated by the nanoparticle, Γ_0 is the decay rate of the donor in free space, R_0 is the Förster radius for an orientational factor equal to one, R_A is the distance of the acceptor to the nanoparticle, R_D the distance of the donor to the nanoparticle, and R_p is the *polarization coupling radius* [5] which describes the influence of the nanoparticle on the FRET rate meditated by the nanoparticle. This distance R_p defines an influence radius of the nanoparticle, it allows to compare the indirect FRET rate (i.e., mediated by the nanoparticle) and the standard free-space FRET rate Γ_{DA}^0.

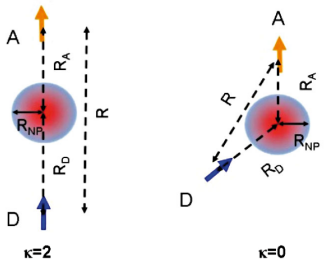

Fig. 2 > Two canonical configurations of the tree body system Donor-NP-Acceptor studied in the present work. (a) Left panel: Aligned configuration. (b) Right panel: Orthogonal configuration. The arrows illustrate the molecular dipole orientations.

For the sake of illustration, let us consider the situation in which the three bodies are aligned with $R_D=R_A=2R_{NP}$, and the transition dipole are aligned in the same direction [see Fig. 2(a)], in this case, we obtain

$$\frac{\Gamma_{DA}^{NP}}{\Gamma_{DA}^0} = \frac{1}{4}\left(\frac{R_p}{R_{NP}}\right)^6$$

where R_{NP} is the radius of the nanoparticle. This simple expression shows that the ratio R_p/R_{NP} is the crucial parameter that describes the influence of the nanoparticle on the FRET rate. For $R_p>R_{NP}$, the nanoparticle enhances the FRET transfer, while for $R_p<<R_{NP}$, the FRET becomes exclusively driven by the direct transfer. Moreover, in previous work [5], we have shown that in the condition that the polarizability of the nanoparticle $\alpha(\omega)$ varies smoothly on the frequency range of the spectral overlap between absorption cross section of the acceptor and the normalized emission spectrum of the donor, the polarization coupling radius R_p depends only on the polarizability tensor of the nanoparticle.

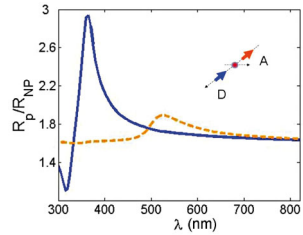

Fig. 3 > Ratio R_p/R_{NP} for Iron (blue solid line), Nickel (gold dash-dotted line), and Cobalt (red dashed line) as a function of the emission wavelength lof the λ donor. R_{NP}=10 nm. The configuration is illustrated in the inset, showing that the dipole are collinear and the couple Donor-Acceptor and nanoparticle are aligned.

We illustrate the formalism for the well-known metallic nanoparticle. Noble metals are known to hold plasmon resonances that enhance, for example, the polarizability of a nanoparticle. Since the polarization coupling radius R_p directly depends on the polarizability, one can expect a substantial influence of the plasmon resonance on the FRET rate mediated by the nanoparticle. This is indeed what we observe in Fig. 3, in which we have plotted the ratio R_p/R_{NP} (with R_{NP}=10 nm) versus the emission wavelength of the donor for gold and silver that are common materials in studies of fluorescence enhancement or quenching. The plasmon resonance is visible in both cases,

leading to an enhancement of R_p/R_{NP}. For instance in the case of silver, one reaches $R_p/R_{NP} \simeq 3$; for gold one has $R_p/R_{NP} \simeq 1.9$. In the particular conditions $R_D = R_A = 2\ R_{NP}$ and $R = 4\ R_{NP}$, we obtain an enhancement factor $\Gamma_{DA}^{NP} / \Gamma_{DA}^{0}$ of the FRET rate on the order of 180 for silver and $\Gamma_{DA}^{NP} / \Gamma_{DA}^{0} \simeq 10$ for gold. For a D-A couple working at plasmon resonance with these materials, we conclude that FRET is mainly driven by the nanoparticle. Incidentally, any change of the dielectric property of the nanoparticle will be reflected in a modulation of the FRET rate. Modulation of the dielectric response can be achieved, for example, through the magneto-optical effect that we consider in the following.

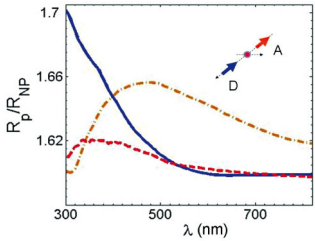

Fig. 4 > Ratio R_p/R_{NP} for Iron (blue solid line), Nickel (gold dash-dotted line), and Cobalt (red dashed line) as a function of the emission wavelength λ of the donor. R_{NP}=10 nm. The configuration is illustrated in the inset, showing that the dipole are collinear and the couple Donor-Acceptor and nanoparticle are aligned. (b) Right panel: Canonical orthogonal configuration.

Using experimental data for the dielectric function of different magneto-optical materials [6], we compute the polarization coupling radius R_p normalized by the nanoparticle radius R_{NP} as a function of several parameters: The emission wavelength of the donor, the radius of the nanoparticle, and the material properties.

Ferromagnetic materials are materials with magnetic anisotropy. Magnetic anisotropy is a consequence of the different directions of magnetization of the different magnetization domains. At saturation, small nanoparticles are customarily considered owning a single domain. This change in magnetization comes

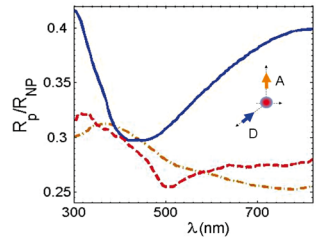

Fig. 5 > Ratio R_p / R_{NP} for Iron (blue solid line), Nickel (yellow dash-dotted line), and Cobalt (red dashed line) as a function of the emission wavelength λ of the donor in the presence of an external magnetic field inducing a magnetization in the direction orthogonal of the plane containing the tree body D-A-NP. R_{NP} =10 nm. The configuration is illustrated in the inset.

with a change of the optical dielectric response (anisotropic response). Therefore ferromagnetic particles own an anisotropic dielectric response controlled by an external magnetic field.

Fig. 4 is an illustration of the ratio R_p/R_{NP} (with R_{NP} =10 nm) versus the emission wavelength of the donor for different standard magneto-optical materials: Nickel, Iron and Cobalt in an aligned configuration (see Fig. 2(a) for a sketch of the geometry). We observe a smoother behavior than in the case of noble metals. Its origin lie in the stronger plasmon damping of magneto-optical materials comparing to metallic materials. For these materials, the amplification factor is around twenty, therefore in this configuration, the FRET rate is still govern by the nanoparticle.

Figure 5 shows a computation of the ratio R_p/R_{NP} with the same materials as in Fig. 4, but in the case of an orthogonal configuration [see Fig. 2(b) for a sketch of the orthogonal geometry]. The magnetization is orthogonal to the plane containing the D-A couple and the nanoparticle. Let us stress that in this configuration the FRET rate vanishes in absence of an external static magnetic field due to the orthogonality of the donor and acceptor transition dipoles. Although one observes that R_p/R_{NP} remains smaller than one, the possibility of inducing a FRET rate driven only by the polarization anisotropy of the

nanoparticle is an interesting result, showing the potential of magneto-optical nanoparticles for FRET. On the one hand, the anisotropic response allows us to couple molecules for which standard FRET gives a vanishing signal due to orientational mismatch (orthogonal transition dipole). On the other hand, the possibility of controlling the magneto-optical response with a static magnetic field as an external parameter could allow us to tune or modulate the FRET rate, which can be an advantage, for example, to increase the sensitivity of the detection process.

We have elucidated the Förster energy transfer problem in a three body configuration, involving two fluorophores close to a nanoparticle with an anisotropic dielectric response. We have shown that the distance dependence is controlled by the Förster radius and a new distance that depends of the polarization properties of the nanoparticle. We have illustrated the effects in the case of a magneto-optical nanoparticle for which the degree of anisotropy can be controlled by an external static magnetic field, and we have discussed potential application for FRET tuning and modulation. Here, we have presented a proof of concept. Further work should focus on enhancing the (weak) magneto-optical FRET signal. We have illustrated the effect also for the well known metallic nanoparticle, showing that it furnishes insight in the understanding of the good quantities controlling this process.

References

[1] T. Förster, Ann. Phys. 437, 55 (1948); Discuss. Faraday Soc. 27, 7 (1959).

[2] L. Stryer, Annu. Rev. Biochem. 47, 819 (1978).

[3] L. Novotny, B. Hecht, Principles of Nano-optics, Cambridge University Press, (2006).

[4] D. L. Dexter, J. Chem. Phys. 21, 836 (1953).

[5] R. Vincent, and R. Carminati, Magneto-optical control of Förster energy transfer, Phys. Rev. B 83, 165426 (2011).

[6] E. D. Palik, Handbook of Optical Constants of Solids (Academic, New York, 1985). ✱

instituto IMdea nanociencia

www.nanociencia.imdea.org

RESEARCH PROGRAMMES

- Molecular nanoscience

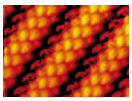
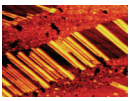

- Scanning probe microscopies and surfaces

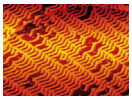
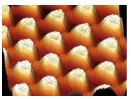

- Nanomagnetism

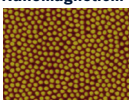
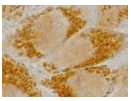

- Nanobiosystems: biomachines and manipulation of macromolecules

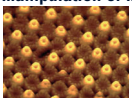


- Nanoelectronics and superconductivity


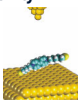
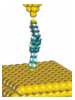

- Semiconducting nanostructures and nanophotonics

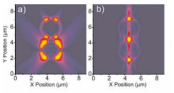

- Nanofabrication and advanced instrumentation


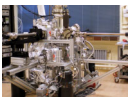

IMDEA-Nanociencia is a private Foundation created by joint initiative of the Comunidad de Madrid and the Ministry of Education of the Government of Spain in February 2007 to manage a new research Institute in Nanoscience and Nanotechnology (IMDEA-Nanociencia). The Institute is located at the campus of the Universidad Autónoma de Madrid in Cantoblanco.

The Institute aims at performing research of excellence in selected areas and offers attractive opportunities to develop a career in science at various levels from Ph.D. students to senior staff positions.

The Madrid Institute for Advanced Studies in Nanoscience also develops an important program of technology transfer and creation of spin-off companies.

E-mail contacto.nanociencia@imdea.org
Phone 34 91 497 68 49 / 68 51
Fax 34 91 497 68 55

GOBIERNO DE ESPAÑA · MINISTERIO DE CIENCIA E INNOVACIÓN

La Suma de Todos
Comunidad de Madrid
www.madrid.org

UNIÓN EUROPEA
FONDOS ESTRUCTURALES

[Nanociencia y Nanotecnología: lo pequeño es diferente
Nanoscience and Nanotechnology: small is different]

instituto IMdea
instituto madrileño de estudios avanzados

Internal electromagnetic field distribution and magneto-optical activity of metal and metal-dielectric magnetoplasmonic nanodisks

D. Meneses-Rodríguez, E. Ferreiro-Vila, J.C. Banthí, P. Prieto, J. Anguita, A. García-Martín, M. U. González, J. M. García-Martín, A. Cebollada and G. Armelles

IMM-Instituto de Microelectrónica de Madrid (CNM-CSIC), Isaac Newton 8, PTM, E-28760 Tres Cantos (Madrid), Spain.

david.meneses@imm.cnm.csic.es

Localized surface plasmon resonances (LSPRs) greatly influence the optical [1-4] and magneto-optical (MO) [5-10] properties of fully metallic and metal-dielectric nanostructures. The observed enhancement in the MO activity when these LSPRs are excited is attributed to the high intensity of the electromagnetic (EM) field inside the global nanostructure when the LSPR occurs [5,11]. Unfortunately, it is not straightforward to experimentally determine the intensity of the EM field inside a nanostructure. Here we show how the EM profile related to the LSPR can be probed locally inside the nanostructure by measuring the MO activity of the system as a function of the position a MO active probe (a Co nanolayer) [12]. This will be done in full detail in metallic systems, and preliminary results will also be presented in more complex metal-dielectric magneto-plasmonic nanodiscs.

The magnetoplasmonic nanodisk arrays have been fabricated in large area onto glass substrates by combining colloidal lithography with sputter, thermal and electron beam deposition and lift-off techniques. Typical nanodisk structures are Au/Co/Au/Cr and Au/SiO_2/Co/SiO_2/Au/Ti, for the fully metallic and the metal-dielectric structures respectively, with total heights between 50 and 70 nm and diameters between 110 and 140nm (Figure 1(a)). For the sake of comparison, continuous thin films with identical composition have been also prepared.

The MO activity (Φ) has been obtained by measuring the MO Kerr effect in polar configuration upon normal incidence illumination, previously identifying the optical resonances through extinction spectra. In the fully metallic nanostructures, we find a distinctive evolution as a function of Co position of the MO activity in the nanodiscs compared with that of the continuous layers, with maximum values when the Co layer is located near the top or the bottom of the disks and minimum values in-between due to the LSPR excitation (Figure 1(b)). This behavior is in contrast with the MO activity exhibited by the continuous films, which increases monotonously as the Co layer becomes closer to the top surface. This indicates that the EM field inside the nanodisks exhibits a nonuniform distribution in plasmon resonance conditions. In fact, the Co layer acts as a probe sensing the EM field within the nanodisk, since the MO activity depends on the intensity of such field. Preliminary results on the possible influence of multiple resonances in metal-dielectric magnetoplasmonic nanodiscs will be also presented.

This information could be very relevant for the design of magnetoplasmonic systems offering optimum MO enhancement, for instance for sensing applications where maximum sensitivity is expected in the areas with higher EM field.

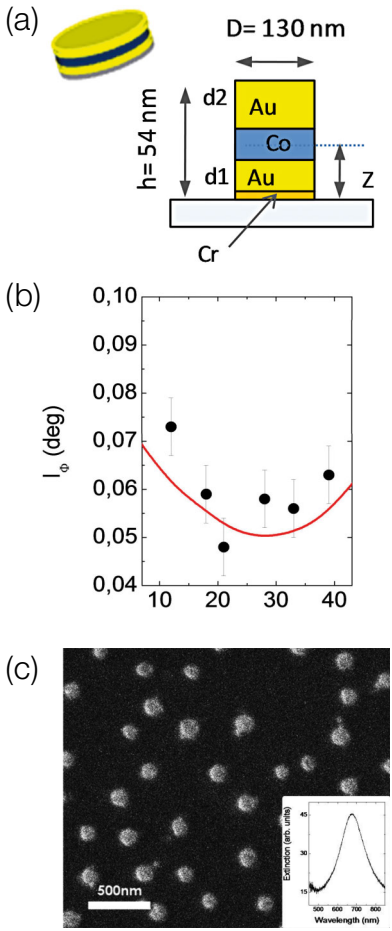

Fig. 1 > (a) Sketch of the fully metallic nanodiscs (b) Maximum magneto-optical activity as a function of the Co position for fully metallic nanodiscs (c) SEM image of an array of metallic nanodisc (Inset: extinction spectrum).

References

[1] S. A. Maier, Plasmonics: Fundamentals and Applications (Springer, Berlin, 2007).

[2] S. A. Maier and H. A. Atwater, J. Appl. Phys. 98, (2005) 011101.

[3] K. H. Su, Q. H. Wei, and X. Zhang, Appl. Phys. Lett. 88 (2006) 063118.

[4] T. Pakizeh, A. Dimitriev, M. S. Abrishamian, N. Granpayeh, and M. Häll, J. Opt. Soc. Am. B 25 (2008) 659.

[5] J. B. González-Díaz, A. García-Martín, J. M. García-Martín, A. Cebollada, G. Armelles, B. Sepúlveda, Y. Alaverdyan and M. Käll, Small 4 (2008) 202.

[6] G. A. Wurtz, W. Hendren, R. Pollard, R. Atkinson, L. Le Guyader, A. Kirilyuk, Th. Rasing, I. I. Smolyaninov and A. V. Zayats, New J. of Phys. 10 (2008) 105012.

[7] P. K. Jain, Y. Xiao, R. Walsworth, and A. E. Cohen, Nanolett. 9 (2009) 1644.

[8] G. X. Du, T. Mori, M. Suzuki, S. Saito, H. Fukuda, and M. Takahashi, Appl. Phys. Lett. 96 (2010) 081915.

[9] L. Wang, K. Yang, C. Clavero, A. J. Nelson, K. J. Karroll, E. E. Carpenter, and R. A. Lukaszew, J. Appl. Phys. 107 (2010) 09B303.

[10] G. X. Du, T. Mori, M. Suzuki, S. Saito, H. Fukuda, and M. Takahashi, J. Appl. Phys. 107 (2010) 09A928.

[11] G. Armelles, A. Cebollada, A. García-Martín, J. M. García-Martín, M. U. González, J. B. González-Díaz, E. Ferreiro-Vila and J. F. Torrado, J. Opt. A: Pure Appl. Opt. 11 (2009) 114023.

[12] D. Meneses-Rodríguez, E. Ferreiro-Vila, P. Prieto, J. Anguita, M. U. González, J. M. García-Martín, A. Cebollada, A. García-Martín and G. Armelles, Small, DOI: 10.1002/smll.201101060 (2011). ✱

Magneto-Optical properties of nanoparticles

R. Gómez-Medina[1], B. García-Cámara[2], I. Suárez-Lacalle[1], L. S. Froufe-Pérez[1], F. González[2], F. Moreno[2], M. Nieto-Vesperinas[3] and J. J. Sáenz[1]

[1] Departamento de Física de la Materia Condensada and Instituto "Nicolás Cabrera", Universidad Autónoma de Madrid, 28049 Madrid, Spain.
[2] Grupo de Óptica, Departamento de Física Aplicada, Universidad Cantabria, 39005 Santander, Spain.
[3] Instituto de Ciencia de Materiales de Madrid, C.S.I.C., Campus de Cantoblanco, 28049 Madrid, Spain.
juanjo.saenz@uam.es

Electromagnetic scattering from nanometer-scale objects has long been a topic of large interest and relevance to fields from astrophysics or meteorology to biophysics, medicine and material science [1-5]. In the last few years, small particles with resonant magnetic properties are being explored as constitutive elements of new metamaterials and devices. The studies in the field often involve randomly distributed small elements or particles where the dipole approximation may be sufficient to describe the optical response. We will discuss the optical response of disordered nano-materials where the constitutive nanoparticles can have a non-negligible response to static (Magneto-Optical active nanoparticles) or dynamic (Magneto-dielectric nanoparticles) magnetic fields.

We will first analyze the peculiar scattering properties of single nanoparticles. In particular, we derive the radiative corrections to the polarizability tensor of anisotropic particles, a fundamental issue to understand the energy balance between absorption and scattering processes [1]. As we will show, Magneto optical Kerr effects in non-absorbing nanoparticles with magneto-optical activity arise as a consequence of radiative corrections to the electrostatic polarizability tensor.

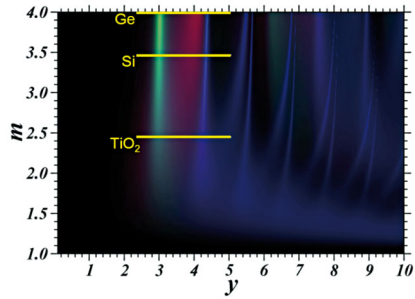

Fig. 1 > Scattering cross section map of a non-absorbing Mie sphere as a function of the refractive index m and the y parameter, y = mka = m(2πa/λ). Green areas correspond to parameter ranges where the magnetic dipole contribution dominates the total scattering cross section, while red areas represent regions where the electric dipole contribution is dominating. Higher order multipoles dominate the remaining blue-saturated areas. (Adapted from Ref. [2]).

We will also explore the properties of high-permittivity dielectric particles with resonant magnetic properties as constitutive elements of new metamaterials and devices [2]. Magnetic properties of low-loss dielectric nanoparticles in the visible or infrared are not expected due to intrinsic low refractive index of optical media in these regimes. Here we analyze the dipolar electric and magnetic response of lossless dielectric spheres made of moderate permittivity materials. For low material refractive index there are no sharp resonances due to strong overlapping between different multipole contributions. However, we find that Silicon particles with index of refraction ~3.5 and radius ~200nm present strong electric and magnetic dipolar resonances in telecom and near-infrared frequencies, (i.e. at wavelengths ≈ 1.2 – 2 μm)

without spectral overlap with quadrupolar and higher order resonances. The light scattered by these Si particles can then be perfectly described by dipolar electric and magnetic fields.

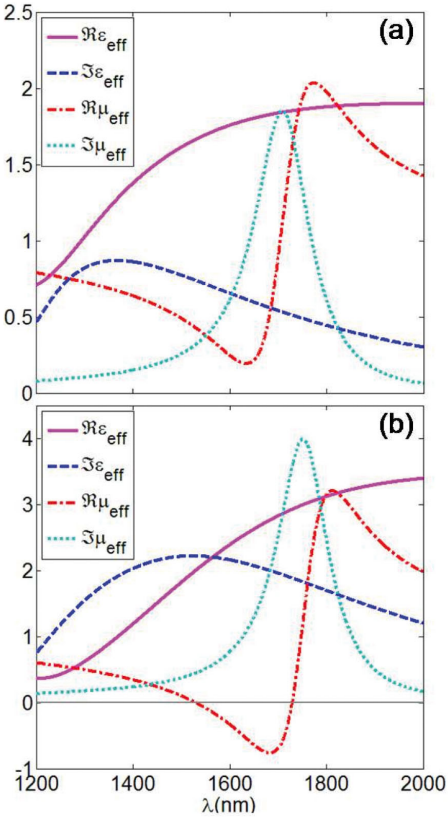

Fig. 2 > Effective real and imaginary permittivities and permeabilities for an arbitrary arrangement of Si spheres in an otherwise homogeneous medium with $\varepsilon_h = \mu_h = 1$ for two different filling factors f = 0.25 (a) and f = 0.5 (b). (From Ref. [2]).

As we will see, the striking characteristics of the scattering diagram of small magneto-optical and magnetodielectric particles [3,4] lead to a number of non-conventional effects in the optical response of nanostructured magneto-optical structures.

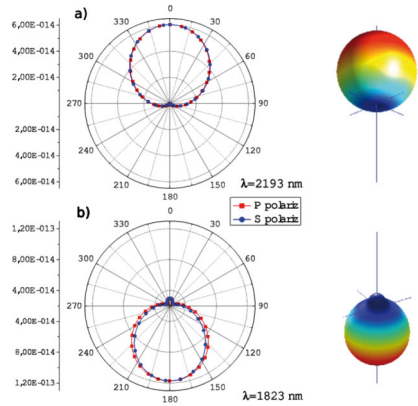

Fig. 3 > Scattering diagrams for a Ge nanosphere with 240nm radius (After Ref. [4]).

Acknowledgments

We appreciate interesting discussions with J. Aizpurua, S. Albaladejo, P. Albella, A. García-Etxarri, M.I. Marqués and F. Scheffold. This work has been sup- ported by the EU NMP3-SL-2008-214107-Nanomagma, the Spanish MICINN Consolider NanoLight (CSD2007-00046), FIS2010-21984, FIS2009-13430-C01-C02, and FIS2007-60158, as well as by the Comunidad de Madrid Microseres- CM (S2009/TIC-1476).

References

[1] S. Albaladejo,R. Gómez-Medina, L. S. Froufe-Pérez, H. Marinchio, R. Carminati, J. F. Torrado, G. Armelles, A. García-Martín and J.J. Sáenz, Opt. Express 18 (2010) 3556.

[2] A. García-Etxarri, R. Gómez-Medina, L. S. Froufe-Pérez, C. López, L. Chantada, F. Scheffold, J. Aizpurúa, M. Nieto-Vesperinas and J. J. Sáenz, Opt. Express 19, 4815 (2011).

[3] M. Nieto-Vesperinas, R. Gómez-Medina, and J. J. Sáenz, J. Opt. Soc. Am. A 28 (2011) 54.

[4] R. Gómez-Medina, B. García-Cámara, I. Suárez-Lacalle, F. González, F. Moreno, M. Nieto-Vesperinas, J. J. Sáenz, J. Nanophoton. 5, 053512 (2011). ✱

Three-dimensional optical metamaterials and nanoantennas: Chirality, Coupling, and Sensing

Harald Giessen

4th Physics Institute, University of Stuttgart,
D-70569 Stuttgart, Germany.
giessen@physik.uni-stuttgart.de

Metallic metamaterials have shown a number of fascinating properties over the last few years. A negative refractive index, negative refraction, superlenses, and optical cloaking are some of the ambitious applications where metamaterials hold great promise.

We are going to present fabrication methods for the manufacturing of 3D metamaterials [1]. We are investigating their coupling properties and the resulting optical spectra. Hybridization of the electric [2] as well as the magnetic [3] resonances allows us to easily understand the complex optical properties. Lateral as well as vertical coupling can result in Fano-resonances [4] and EIT-like phenomena [5, 6]. These phenomena allow to construct novel LSPR sensors with a figure of merit as high as five [7].

The connection between structural symmetry and their electric as well as magnetic dipole and higher-order multipole coupling will be elucidated. It turns out that stereometamaterials [8], where the spatial arrangement of the constituents is varied (see figure), reveal a highly complex rotational dispersion. The chiral properties are quite intriguing and can be explained by a coupled oscillator model.

Our three-dimensional stacking approach allows also for the fabrication of 3D nanoantennas, which are favorable for emitting and receiving radiation from quantum systems [9].

References

[1] Na Liu, Hongcang Guo, Liwei Fu, Stefan Kaiser, Heinz Schweizer, and Harald Giessen: Three-dimensional photonic metamaterials at optical frequencies, Nature Materials 7, 31 (2008).

[2] N. Liu, H. Guo, L. Fu, S. Kaiser, H. Schweizer, and H. Giessen: Plasmon Hybridization in Stacked Cut-Wire Metamaterials, Advanced Materials 19, 3628 (2007).

[3] Na Liu, Liwei Fu, Stefan Kaiser, Heinz Schweizer, and Harald Giessen: Plasmonic Building Blocks for Magnetic Molecules in Three-Dimensional Optical Metamaterials, Advanced Materials 20, 3859 (2008).

[4] B. Lukyanchuk, N. I. Zheludev, S. A. Maier, N. J. Halas, P. Nordlander, H. Giessen, and C. T. Chong: The Fano resonance in plasmonic nanostructures and metamaterials, Nature Materials 9, 707 (2010).

[5] Na Liu, Stefan Kaiser, and Harald Giessen: Magnetoinductive and Electroinductive Coupling in Plasmonic Metamaterial Molecules, Advanced Materials 20, 4521 (2008).

[6] Na Liu, N. Liu, L. Langguth, T. Weiss, J. Kästel, M. Fleischhauer, T. Pfau, and H. Giessen: Plasmonic EIT analog at the Drude damping limit, Nature Materials 8, 758 (2009).

[7] Na Liu, T. Weiss, M. Mesch, L. Langguth, U. Eigenthaler, M. Hirschner, C. Sönnichsen, and H. Giessen: Planar metamaterial analog of electromagnetically induced transparency for plasmonic sensing, Nano Lett. 10, 1103 (2010).

[8] Na Liu, Hui Liu, Shining Zhu, and Harald Giessen: Stereometamaterials, Nature Photonics 3, 157 (2009).

[9] H. Giessen and M. Lippitz: Directing light emission from quantum dots, Science 329, 910 (2010). *

Spin transfer RF nano-oscillators for wireless communications and microwave assisted magnetic recording

U. Ebels[1], M. Quinsat[1,2], D. Gusakova[1], J. F. Sierra[1], JP Michel[1,2] , D. Houssameddine[1], B. Delaet[2], M.-C. Cyrille[2], L. D. Buda-Prejbeanu[1,3], B. Dieny[1]

[1] SPINTEC, UMR(8191) CEA / CNRS / UJF / Grenoble INP ; INAC, 17 rue des Martyrs, 38054 Grenoble Cedex, France.
[2] CEA-LETI, MINATEC, 17 Rue des Martyrs, 38054 Grenoble, France.
[3] Grenoble INP, 46, Avenue Félix Viallet, 38031 Grenoble Cedex 1, France.

Slonczewski [1] and Berger [2] predicted in 1996 that a spin-polarized current flowing through a magnetic nanostructure exerts a torque on its magnetization due to the exchange interaction between the spin of the conduction electrons and the spin of the electrons responsible for the local magnetization. This torque is called spin transfer torque (STT). The possibility to use the STT to switch the magnetization of a magnetic nanostructure was first experimentally observed in metallic spin-valve nanopillars [3] and later in magnetic tunnel junctions [4]. The spin torque acts as a damping or antidamping term and can induce very peculiar magnetization dynamics. Of particular interest is when an applied field and the spin transfer torque (STT) have competing influence on the magnetization of the free layer of a spin-valve or of a magnetic tunnel junction, for instance the field favoring parallel alignment between the magnetization of the free layer magnetization and that of the reference layer whereas the STT favors antiparallel alignment. In such situations, the magnetization of the free layer is driven into steady state oscillations. The magnetization continuously pumps energy into the spin current to compensate the dissipation due to Gilbert damping. These steady state oscillations combined with the giant or tunnel magnetoresistance of the stack generate oscillations of the voltage across the stack at GHz frequencies. Moreover the frequency varies as a function of the current density flowing through the stack.

This phenomenon can be used to design frequency tunable RF oscillators which could be quite useful in a number of devices such as RF STT oscillators (STO) for wireless communications, or as microwave generators to assist the writing by microwaves in magnetic recording technology or as magnetic field sensors taking advantage of the shift of frequency induced by an applied magnetic field.

In this paper, our R&D efforts on STT RF oscillators as well as current trends in this field are described.

A significant effort has been focused on a particular configuration of STT RF oscillators in which an out-of-plane magnetized polarizer is used to inject out-of-plane spin polarized electrons into an in-plane magnetized free layer [5]. Indeed, it was shown that this configuration is particularly interesting since it allows generating large angle precessional motion thereby maximizing the magnetoresistance signal associated with this motion[5]. In this configuration, the frequency varies almost linearly with current up to a maximum value where it saturates because of micromagnetic distorsion of the magnetization.

Two important characteristics must be carefully addressed in such oscillators before being able to use them in RF devices for wireless communications. One is the output power, the other is the excitation linewidth and associated phase noise.

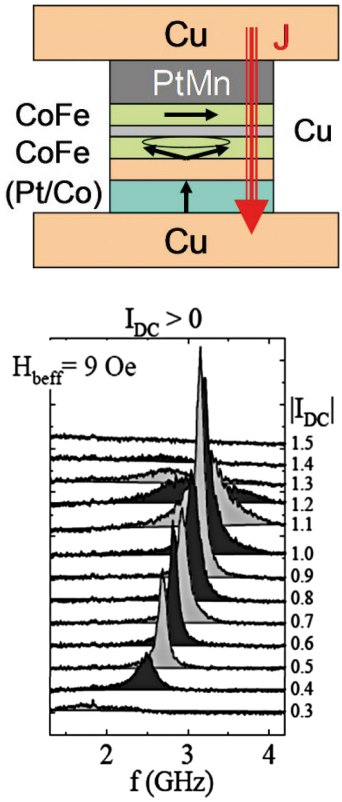

Fig. 1 > STT oscillator with perpendicular polarizer and in-plane free layer. A fixed in-plane magnetized reference layer is added to produce a magnetoresistance between this reference layer and the precessing free layer. Typical spectra obtained when measuring the RF voltage between top and bottom electrodes. The oscillator pillar has typical diameter between 150nm and 50nm.

By using magnetic tunnel junctions, the output power could be increased by 2 orders of magnitude thanks to the higher impedance of these systems [6,7]. Recently, output powers of the order of 1 µV were reported in STT oscillator based on magnetic tunnel junction and exploiting a vortex configuration of magnetization [6]. Although the frequency associated with these vortex based STO is too low for practical applications (300MHz-1GHz), these results demonstrate the possibility to increase the output powers to acceptable value for this type of applications thanks to the use of magnetic tunnel junctions.

Concerning the linewidth and phase noise, several studies have aimed at understanding the cause of the linewidth in STO oscillators in order to try increasing the coherence of the magnetization dynamics and thereby minimize the excitation linewidth and phase noise. Frequency and time-domain characterizations were performed. As an example, Figure 2 shows time domain measurements performed on MgO magnetic tunnel junction (MTJ) pillars [7]. The RF voltage was measured between the top and bottom electrodes of the MTJ while a DC current I flows through the pillar. Figure 2 clearly shows that the STT induced magnetic excitations start above a current threshold. However, the excitations first appear in bursts (region 2). As the current is further increased, the excitations become more and more persistent.

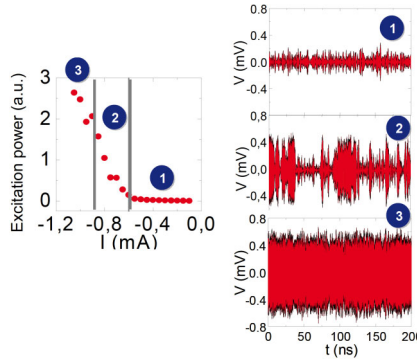

Fig. 2 > Time domain measurements of the RF voltage induced by STT excitations in a MgO based MTJ submitted to a DC current. Left: Power of excitations versus DC current amplitude. Right: real time voltage measurements for three different values of the DC current flowing through the MTJ.

By performing a Fourier transform over a sliding time window of 10ns of the RF voltage associated with these steady state excitations,

it appears that the excitation frequency is not stable but fluctuates (see the spectrogram in Fig. 3).

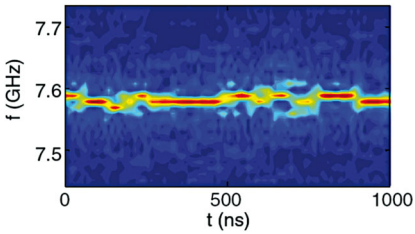

Fig. 3 > Spectrogram obtained by a Fourier transform over a sliding time window of 10ns of the real-time RF voltage shown in Fig. 2, regime 3.

These frequency fluctuations can have different origins. One is the influence of the thermal activation k_BT. Random thermal fluctuations perturb the modes which are excited by STT, temporarily changing the magnetization dynamics. Furthermore, the magnetization dynamics under STT is highly non-linear. The non-linearity, as in systems prone to chaotic behavior, can lead to unstable magnetization dynamics. Furthermore the non-linearity also causes the frequency to depend on the amplitude of the excitations which may also participate to the fluctuations seen in Fig. 3.

By optimizing the structure of the stack and for instance using synthetic antiferromagnetic free layer, the linewidth could be also significantly reduced.

Another area where these STT oscillators can be quite useful is the one of magnetic recording. The present technology of recording which consists in storing the information on granular media and switching the magnetization of the grains with a write head which is a tiny electromagnet, is reaching a physical limit called the magnetic trilemma. This trilemma is caused by the impossibility to satisfy simultaneously i) a sufficient stability of the magnetization of the grains in the media against thermal fluctuations, ii) a sufficient media signal to noise ratio and iii) the ability to write on the media with magnetic field which can be produced by the write head (maximum produced field by the write head of the order of 2T).

It was therefore proposed to assist the writing either with a temporary heating of the media (Heat Assisted Magnetic Recording: HAMR) or by microwave (Microwave Assisted Magnetic Recording: MAMR).

In MAMR a spin-transfer oscillator is inserted in the write gap of the head. This oscillator has also a perpendicular to plane polarizer combined with and in-plane magnetized free layer. However, it has no reference layer since its purpose is to generate a RF field outside the pillar (i.e. on the media, where the bit has to be written) and not a RF voltage across the pillar. The precession of the free layer generates a rotating dipolar RF field outside the nano-oscillator pillar. This RF field penetrates into the media and transfer energy to the magnetization of the grains. This additional energy combined with the field from the write pole of the head allows the switching of the magnetization of the media. This technology is under development in most major Hard Disk Drive companies. The difficulties are too produce enough RF power at a frequency of the order of 30 to 40GHz close to the FMR frequencies of high anisotropy magnetic media and ensure that this power is primarily absorbed in the media and not in the surrounding magnetic environment, particularly the writing pole and trailing shield.

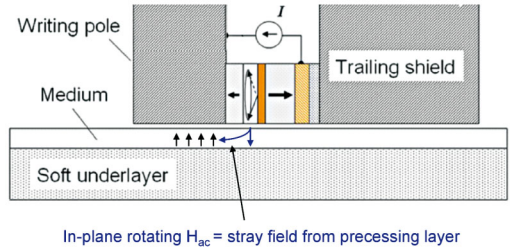

Fig. 4 > Schematic representation of the operation principle of MAMR.

Another area of increasing interest concerning STO is the one of magnetic field sensors. The basic idea is to use the dependence of the oscillation frequency of STO on the applied field to measure the amplitude of the applied field [8]. Figure 5 illustrates the variation f(H) in a spin-valve structure traversed by a DC current. The magnetization of the soft layer is driven into steady state oscillations. The giant magnetoresistance of the stack then produces an oscillatory voltage between top and bottom electrodes [9]. The shift of frequency versus applied field can be quite steep, as large as 180GHz/T [10]. With an appropriate frequency modulation detection scheme, this approach could allow the realization of very small magnetic field sensors sub-30nm*30nm which could replace TMR sensors in read heads of HDD.

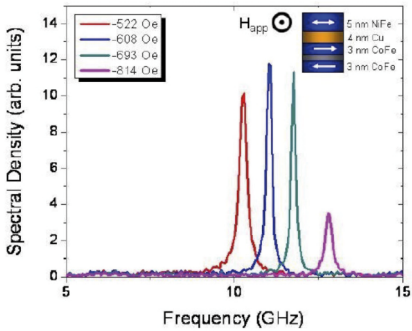

Fig. 5 > Shift of frequency versus applied field measured in a spin-valve based STO. From Ref.[9].

References

[1] Slonczewski, J., "Currents and torques in metallic magnetic multilayers", J.Magn.Magn. Mater.159, L1 (1996).

[2] Berger, L., Phys.Rev.B 54, 9353 (1996).

[3] Katine, J.A., Albert, F.J ., Buhrman, R.A., Myers, E.B., and Ralph, D.C, Phys.Rev.Lett.84, 3149 (2000).

[4] Y.Huai et al, Appl.Phys.Lett.84 (2004), 3118.

[5] D. Houssameddine, U. Ebels, B. Delaët, B. Rodmacq, I. Firastrau, F. Ponthenier, M. Brunet, C. Thirion, J. P. Michel, L. D. Buda-Prejbeanu, M. C. Cyrille, O. Redon, and B. Dieny, Nature Materials 6, 447 (2007).

[6] A.Dussaux, B.Georges, J.Grollier, V.Cros, A.V.Khvalkovskiy, A.Fukushima, M.Konoto, H.Kubota, K.Yakushiji , S.Yuasa, etal., Nature Communications 1, 1(2010), ISSN2041-1723.

[7] D. Houssameddine, U. Ebels, B. Dieny, K. Garello, J.-P. Michel, B. Delaet, B. Viala, M.-C. Cyrille, J. A. Katine and D. Mauri, Phys. Rev. Lett. 102, 257202 (2009).

[8] Sato et al, US7 471 491 B2 (2008).

[9] P.M.Braganca, B.A.Gurney, J.A.Katine, S.Maat, J.R.Childress, Nanotechnology 21 (2010) 235202.

[10] N.Stutzke, S.L.Burkett, S.E.Russek, Appl. Phys.Lett.82 (2003) 91.

[11] K.Mizushima,K.Kudo,T.Nagasawa,and R.Sato, Journ.Appl.Phys. 107,063904(2010). *

nanoresearch

Characterization of an electrostatically actuated Pd coated MEMS resonators

J. Henriksson[1], J. Arcamone[2], G. Villanueva[1], J. Brugger[1]

[1] Microsystems Laboratory, EPFL, Lausanne, CH-1015, Switzerland.
[2] CEA, LETI, MINATEC, F-38054 Grenoble, France.
jonas.henriksson@epfl.ch

Introduction

Electrostatically actuated MEMS resonators feature CMOS integrability, ultra-low power consumption and stable readout. To utilize these properties for gas sensing, we fabricated a doubly clamped free-standing beam of amorphous silicon (see Figure 1). A functionalizing layer of palladium is patterned to cover the beam. The Pd also serves as electrical path on the beam. Below the beam, a bottom electrode has been patterned by lift-off.

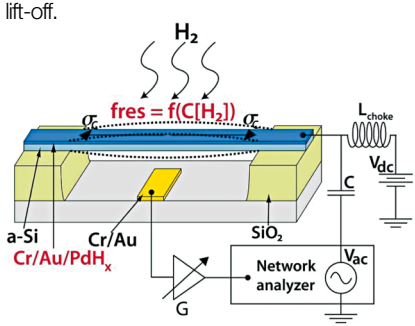

Fig. 1 > Schematic illustrating actuation, readout and sensing principle of the device [1].

By applying an alternating voltage between the beam and the bottom electrode, the beam is brought into resonance. The resonance frequency is measured by monitoring the transmitted signal between the beam and the bottom electrode. The electrical equivalent of this configuration is a RLC branch [2], representing the mechanical motion, in parallel with a capacitance, representing the parallel plate capacitance as well as the capacitance between the electric paths on the chip and wires connecting onto the chip (see Figure 2).

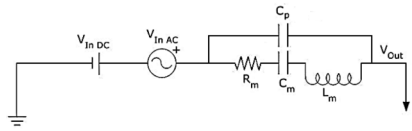

Fig. 2 > The electrical equivalent of the MEMS device.

The sensing principle is based on the fact that Pd expands in the presence of H_2. This property has been used for H_2 sensing in different configurations, such as cantilevers [3-5], chemo-mechanical switches [6, 7] and discontinuous films that form new conductive paths as the grains expand [8, 9].

Micro- and nano-electromechanical resonators excel in the field of sensing applications, showing high sensitivity, low noise susceptibility and precise readout. They are widely used in science and technology for detection of mass [10], temperature [11] and gas pressure [12].

With our design, the idea is to induce a change of stress on the beam through H_2 exposure, thus benefiting from the strong natural phenomenon of H_2 induced Pd expansion.

In this report we investigate a few strategies to improve the quality of the readout signal in order to enhance the sensitivity and robustness of the device.

Background of experiments

The electrostatic interaction between the beam and the bottom electrode can be approximately described as a parallel plate capacitor interaction. In this case, the electrostatic force is given by

$$F_e = \frac{\varepsilon}{2}\frac{A}{d^2}V^2$$

where ε is the permittivity, A is the area, d is the distance and V is the voltage. In our configuration an alternating voltage is ($V_{In\,AC} = V_{AC\,pv}\sin 2\pi f t$) super-positioned with a direct voltage ($V_{In\,DC}$). The voltage term can be developed

$$V^2 = V_{In\,DC}^2 + \frac{V_{AC\,pv}^2}{2}(1-\cos 4\pi f t) + V_{In\,DC}V_{AC\,pv}\sin 2\pi f t$$

Not surprisingly, the direct voltage gives a component which does not vary in time and is redundant with respect to dynamic actuation. The alternating voltage renders variation of force that varies at 2f, twice the frequency of the electric signal frequency. The combined term gives a force component that varies at f, the same frequency as the electric signal frequency. We can thus either actuate at f while simultaneously measuring the response at f, using the latter term, or actuate at f and measure the response at 2f, using the prior term. Which of these strategies is better depends on the characteristics of the device. A common problem is that the feed-through signal (the signal going through C_p) is so large that the resonance peak is impossible to measure. In this case, that feed-through signal will be substantially decreased by applying an actuation voltage at $f_{res}/2$ while measuring at the doubled frequency.

Another approach to reduce feed-through is to connect two identical devices in parallel, while only applying $V_{In\,DC}$ on one of them. Equivalent alternating voltages are applied to the two devices, however 180° phase shifted. Immediately after the devices, the paths reconnect and the feed-through signals cancel out each other due to the difference in phase. Any remaining signal close to resonance frequency is caused by the mechanical motion of the resonator. This approach is called a differential measurement setup.

Measurements at atmospheric pressure differ from those made in vacuum in that the energy losses due to drag forces are higher. To find out how critical this loss mechanism is compared to others, such as clamping losses, we made a comparative experiment.

In addition, we studied the spring softening effect, which is caused by the fact that the electrical force becomes stronger as the inter-electrode distance is decreased during actuation. It is approximated as $k_E = -\frac{\varepsilon_0 A V^2}{x^3}$, leading to a decrease of resonance frequency according to $f_{res} = f_0\left(1-\frac{k_E}{2k}\right)$. Given that the resonating motion originates from the product of V_{ac} and V_{dc}, the resonance frequency is expected to decrease linearly with respect to V_{dc}, giving $f_{res} = f_0 - aV_{dc}$.

Results

Single vs. differential measurements

In Figure 3, the difference in feed-through between single and differential measurement configuration is illustrated. We found that in this case, the magnitude of the feed-through decreased by more than an order of magnitude.

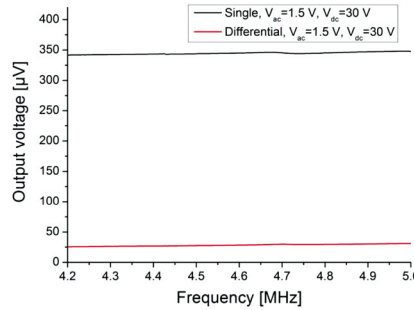

Fig. 3 > Comparison between single and differential configuration (amplitude measurement).

As the differential configuration turned out to be very successful, we used it also for the most experiments.

Spring-softening effect

Figure 4 illustrates what happens when we increase the V_{dc}. We see that the magnitude of

the response increases as V_{dc} is increased. In addition the resonance frequency decreases due to spring-softening.

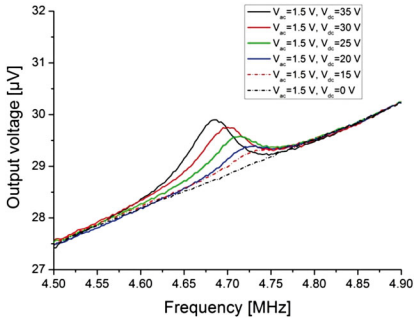

Fig. 4 > Differential measurement in atmospheric pressure, illustrating the increase in magnitude and spring-softening effect as V_{dc} is increased.

The spring softening is approximated as $f_{res} = f_0\left(1 - \frac{k_E}{2k}\right)$, where $k_E = -\frac{\varepsilon_0 A V^2}{x^3}$. Given that the resonating motion originates from the product of V_{ac} and V_{dc}, the resonance frequency is expected to decrease linearly with respect to V_{dc}. Based on a linear relationship ($f_{res} = f_0 - aV_{dc}$), the following coefficients were determined

ΔV_{dc} [V]	Δf_{res} [kHz]	a [kHz/V]
20-15=5	0	0
25-20=5	-12.5	2.5
30-25=5	-12.5	2.5
35-30=5	-12.5	2.5

The change of resonance frequency is thus approximately linear, but changes are very close to the step size frequency increase, which limits the precision.

Atmospheric pressure vs. vacuum

Figure 5a illustrates measurements made under vacuum. Figure 5b illustrates measurements on the very same device but under atmospheric pressure. We find that for equivalent electrostatic forces, the beam in vacuum clearly responds stronger. At V_{dc}=30 V, the beam in atmospheric pressure shows a 1.5 μV magnitude change at resonance whereas the beam in vacuum changes by 5 μV.

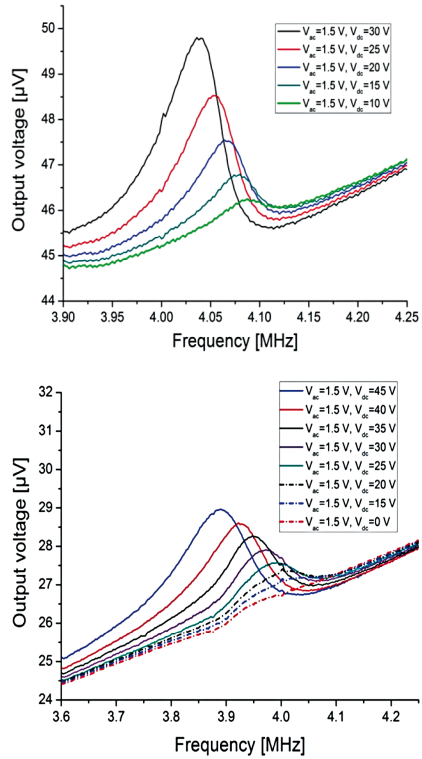

Fig. 5 > Same device a) measurement in vacuum and b) measured in atmospheric pressure.

2f measurements

The result of a 2f measurement is shown in Figure 6. The most important difference is that the background has been attenuated by close to 2 orders of magnitude. The signal-to-background ratio is much more favorable. However, the output signal is also attenuated. As noise is more visible, we find that the signal-to-noise ratio is worse as compared to measurements at f.

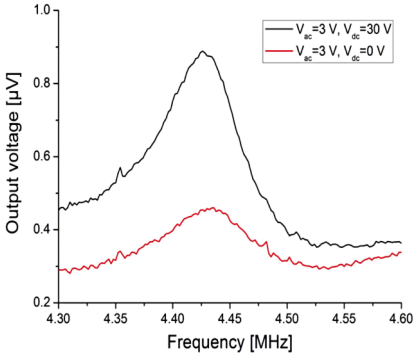

Fig. 6 > 2f measurement.

Conclusions

We have tested several different methods to improve the signal quality of an electrostatically actuated MEMS device. We report that the differential measurement configuration is an effective way to improve the readout signal. A weak spring-softening effect was observed. Comparisons between measurements in vacuum and in atmospheric pressure showed that media-related damping (squeeze damping) is dominant, but the damping caused by the clamping is also considerable. The 2f measurement readout scheme attenuated the background very strongly, as expected, but it is not clear if this is helpful as the signal-to-noise ratio is also decreased.

As an outlook, the next step in improving the readout of the sensor would be to design and fabricate a device with three terminals, so that driving and reading can be separated more efficiently.

References

[1] Henriksson, J., L. G. Villanueva Torrijo, and J. Brugger. Ultra-low power palladium-coated MEMS resonators for hydrogen detection under ambient conditions. in Transducers '11. 2011. Beijing: IEEE.

[2] Arcamone, J., et al., A compact and low-power CMOS circuit for fully integrated NEMS resonators. Ieee Transactions on Circuits and Systems Ii-Express Briefs, 2007. 54(5): p. 377-381.

[3] Baselt, D.R., et al., Design and performance of a microcantilever-based hydrogen sensor. Sensors and Actuators B-Chemical, 2003. 88(2): p. 120-131.

[4] Hu, Z.Y., T. Thundat, and R.J. Warmack, Investigation of adsorption and absorption-induced stresses using microcantilever sensors. JOURNAL OF APPLIED PHYSICS, 2001. 90(1): p. 427-431.

[5] Okuyama, S., et al., Hydrogen Gas Sensing Using a Pd-Coated Cantilever. Jpn. J. Appl. Phys., 2000. 39: p. 3584-3590.

[6] Kiefer, T., et al., A single nanotrench in a palladium microwire for hydrogen detection. Nanotechnology, 2008. 19(12).

[7] Kiefer, T., et al., Large arrays of chemo-mechanical nanoswitches for ultralow-power hydrogen sensing. Journal of Micromechanics and Microengineering, 2010. 20(10).

[8] Xu, T., et al., Self-assembled monolayer-enhanced hydrogen sensing with ultrathin palladium films. APPLIED PHYSICS LETTERS, 2005. 86(20).

[9] Kiefer, T., et al., The transition in hydrogen sensing behavior in noncontinuous palladium films. APPLIED PHYSICS LETTERS, 2010. 97(12).

[10] Naik, A.K., et al., Towards single-molecule nanomechanical mass spectrometry. Nature Nanotechnology, 2009. 4(7): p. 445-450.

[11] Pandey, A.K., et al., Performance of an AuPd micromechanical resonator as a temperature sensor. APPLIED PHYSICS LETTERS, 2010. 96(20).

[12] Huang, X.M.H., et al., Nanomechanical hydrogen sensing. APPLIED PHYSICS LETTERS, 2005. 86(14). *

Optical analysis (study) of InAsP/InP core shell nanowires

Fauzia Jabeen[1], Bernt Ketterer[2], Gilles Patriarche[1], Anna Fontcuberta I Morral[2], Jean-Christophe Harmand[1]

[1] CNRS - Laboratoire de Photonique et de Nanostructures, Route de Nozay, 91460 Marcoussis, France.
[2] Laboratoire des Matériaux Semiconducteurs, Institut des Matériaux, Ecole Polytechnique Fédérale de Lausanne, CH-1015 Lausanne, Switzerland.
fauzia.jabeen@lpn.cnrs.fr

Abstract > InAsP/InP core-shell nanowires (NWs) with a systematically increasing As content are grown by molecular beam epitaxy. The As content in the ternary core part of these NWs is varied in pursuit of obtaining stacking fault free InAsP/InP core-shell NWs and μ – PL analysis is carried out to make a correlation between the improvement in the crystal structure of NWs and their optical properties.

Introduction

Most of the III-V materials exhibit cubic zinc blende (ZB) crystal structure in bulk, whereas one dimensional (1D) structures of the same materials (NWs) often turn out to be hexagonal wurtzite (WZ) crystals with stacking faults, twins and intermixing of ZB and WZ sections. These crystal defects, randomly occurring along the length of the NWs, undermine the optical and electrical properties of NWs (Akopian, 2010), (Minot, 2007). Therefore, for the realization of efficient NWs based devices, it is essential to grow either single crystal structure NWs or controlled heterostructures of ZB and WZ sections. Presence of stacking faults in molecular beam epitaxy grown InP NWs has already been reported (Tchernycheva, 2007). To suppress the stacking faults, a thorough optimization of the growth parameters is required. In a previous study, we observed the absence of stacking faults in the nanowire section where InAsP was inserted. This observation gives a hint of a positive role of the arsenic flux which was supplied for InAsP growth in suppressing such crystal phase mixing.

Here we present a systematic study on MBE-grown $InAs_xP_{1-x}$ NWs. We examine the effects due to variations of *As* content on their crystal structure and optical properties. In order to get good photoluminescence (PL) efficiency the surface states need to be passivated. This can be obtained by growing InP shells around the initial $InAs_xP_{1-x}$ cores. It is well-known that the crystal structure of the shell follows that of the core; i. e. crystal phase of the core-shell (CS) NW is determined during core growth and remains unchanged during shell formation. Therefore growth parameters are optimized for stacking faults free $InAs_xP_{1-x}$ core NWs which are subsequently wrapped with InP. These CS NWs will have better PL efficiency as reported for other NWs systems (Jabeen, 2008), (Wu, 2003).

Experimental details

InAsP/InP CS NWs were grown by molecular beam epitaxy on InP substrates by vapor-liquid-solid mechanism with Au used as catalyst. A thin InP buffer layer was grown on the epi-ready InP substrate for an atomically smooth surface. The growth chamber is equipped with an *in-situ* Au effusion cell. This permits to deposit a controlled amount of catalyst on the as-grown buffer layer, with no risk of surface contamination by ex situ manipulation. Details about the growth parameters, morphology and structural analysis can be found elsewhere (Jabeen,

2011) here we will focus only on the optical studies which were performed on these NWs with a brief description of the NWs structure for two extremes i. e. grown with lowest and highest *As* in the core.

For the low-temperature micro photoluminescence (μ - PL) experiments NWs were transferred mechanically on a Si substrate with markers defined by lithography for easy spotting of individual NWs. This experiment is performed at 10K in a liquid helium flow cryostat by illuminating the sample with Ar+Kr+ or HeNe lasers with wavelengths respectively 647.1nm and 632.8nm and collecting the signal in a Si detector. Laser spot size is <600 nm.

In Fig. 1 scanning transmission electron microscopy (STEM) images acquired by SEM are presented for two extremes. These images are acquired by transferring the NWs on the TEM grids. Fig. 1(a) is InAsP/InP CS NWs with lowest *As* content in the core and these NWs exhibits stacking faults all along the NW. For this low *As* content no CS formation is observed. EDS performed on these NWs results with no *As* incorporation in these NWs or it is the below the detection limit of system used for this experiment. In Fig. 1(b), bottom section of a single NW grown with highest *As* content is shown. CS formation is clearly visible in this image where contrast in the middle part of the NW indicates core part with a diameter of ~10 – 15 nm. No contrast along the NW observed for the whole length indicating the suppression of the stacking faults in these NWs.

In Fig. 2 a sketch of the CS NW is presented to describe how the PL experiment was performed. In order to distinguish that the acquired spectra is from the base or the tip of the NW, NWs are measured at three different points. At the base, it is expected to have a contribution from the core as well as the shell, at the middle part, where depending on the length of the NW and point of detachment from the substrate, the spectra can have the contribution from core or not and emission

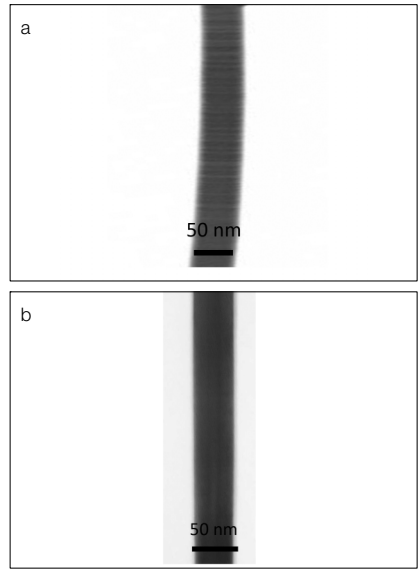

Fig. 1 > (a) Scanning transmission, electron microscopy (STEM) images of the InAsP/InP CS NWs. In (a) CS NWs grown with lowest As/P ratio exhibiting stacking faults all along the NW length. In (b) NW from the sample grown with highest As/P ratio and resulting NW with a clear core of 10 – 15 nm diameter with a shell around but no stacking faults arte observed.

related to shell for all the NWs and at the tip, where only shell related emission is expected. Hence for all the analyzed NWs, for comparison, spectra acquired at the base are taken into account.

μ – Photoluminescence

μ – PL spectra were acquired on several single NWs for each sample grown with different *As* content in the InAsP core part. First we focus on the PL spectra related to the InP emission energy range. μ – PL spectrum recorded for a single NW with lowest *As* is shown in black color in Fig. 3(a). Broad PL spectrum lies within the range of emission energy for InP with mixed crystal structure [(Jancu, 2010), (Pemasiri, 2009), (Bao,

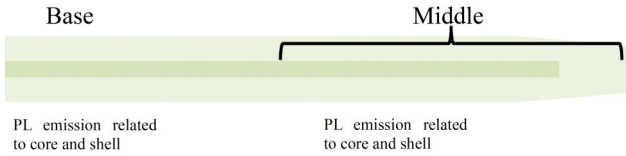

Fig. 2 > Sketch of CS NW in the top part indicating three parts where PL spectra are acquired and expected emissions related to core and shell part.

2008), (Titova, 2007)]. The splitting of the peaks, which is the reasons for the emission peaks at various energy values, indicate the presence of randomly varying ZB and WZ sections thicknesses within the InP emission energy range as reported by Jancu and co authors [(Jancu, 2010), (Pemasiri, 2009)]. Other NWs studied from the same sample (not shown) emits in the similar wavelengths range and spectra were always composed of several peaks with different weights within the energy range related to InP. Red color in Fig. 3(a), represent the μ - PL spectra from the sample grown with 0.38 As/P ratio. This spectrum is comprised of a broad peak centered at 1.447 eV along with shoulders at higher energy corresponding to emission from InP. PL spectra acquired on NWs from this sample emits within this energy range but contains many peaks.

μ – PL spectra obtained for the NWs grown with 0.51 As/P ratio are represented by green color in fig 3(a). Since these NWs show fewer stacking faults compared to previous samples (not shown here) main peak corresponding to InP is at 1.442 eV with a shoulder at 1.48 eV. Several NWs measured from this sample exhibits less inhomogeneity. Recorded PL spectra show some sharp lines distributed between this energy ranges suggest the insertions of certain number of monolayer of WZ and ZB segments for all measured NWs from this sample. Finally, sample with highest *As* content and no stacking faults as shown in Fig. 1(b) is measured. Blue line in Fig. 3(a) represent PL spectra from a NW from the sample with highest *As* content. An emission peak, at 1.43 eV, is recorded for this sample. All the NWs measured from this samples emits at this energy value indicating highly homogeneous NWs. In Fig. 3(b) full width half maximum (FWHM) for these spectra is plotted. Decrease in FWHM with increasing *As* content in the core of these NWs gives a direct evidence of improvement in the crystal quality of these NWs.

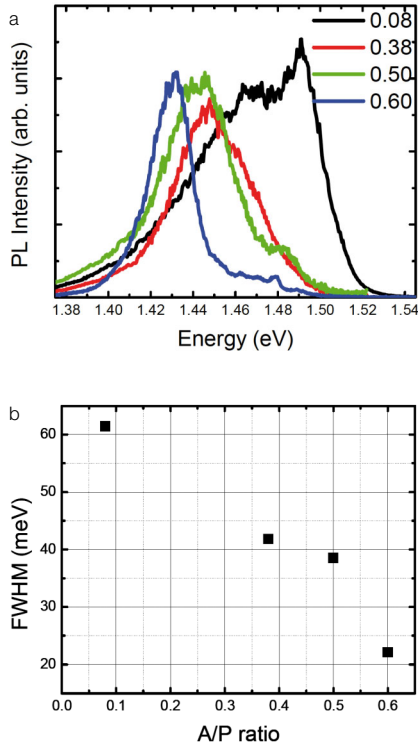

Fig. 3 > μ - PL spectra acquired on single NWs for each sample. Broader PL emission (black line) for lowest As/P content indicates the phase mixing, whereas decreasing FWHM of the PL peaks with increasing As content indicate an improvement in the crystal quality as presented in (b).

Concerning the PL emission related to the core of the NWs, acquired spectra at the base of all the NWs are plotted in Fig. 4. The spread of the emission energy is between 1.35eV – 1.221 eV which indicate an increase in the *As* content in the core of these NWs. For the emission from NWs grown with 0.38 As/P ratio, shown in Fig. 4 in red line, a broad peak is observed. The possible reason of this broad peak could be the variations in the thicknesses of WZ and ZB segments which results in the emission at several energies value within a certain range. From one NW to other NW, shift in observe peak position shift within the same energy range. For few NWs, sharp peaks are observed, indicating either repetition of ZB and WZ section lengths or non homogeneous As incorporation in the core. This splitting is not a general trend for all the measured NWs for this sample and it could be due to the presence of a closely attached another NW. In Fig. 4, green line represents the PL emission for NWs grown with 0.50 As/P ratio. Here again a broad peak is recorded with an emission between 1.35 eV – 1.25 eV. For all the measured NWs from this sample, as in case of InP shell for this sample, emission peaks are at the similar energies. This indicates a step towards homogeneity in NWs but the broad spectra indicate presence of stacking faults. NWs sample with highest *As* content, plotted in blue line in Fig. 4, emit at 1.217 eV with all the measured NWs emitting around this energy. This homogeneity in the emission energy has also been observed for the shell of these NWs and it gives a further weight to the fact that these NWs are of good crystal quality. Another indication is the decrease in FWHM of the emission spectra with increasing *As* content in the core. In the set at the top left of the Fig. 4, FWHM for these samples related to the core emission PL peaks is plotted.

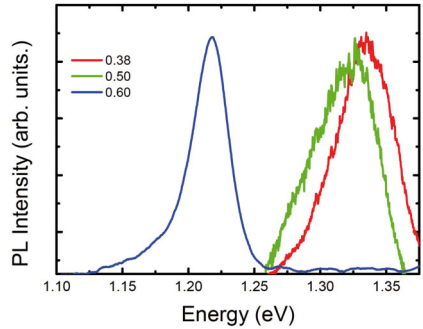

Fig. 4 > μ - PL spectrum corresponding to the InAsP core with increasing As/P ratio. Blue shift in energy indicate an increase in the As content in the InAsP core. In the top left an inset regarding the FWHM of these emission peaks is plotted as a function of the As/P ratio. Decreasing FWHM indicate improvement in overall crystal quality of observed NWs.

Discussion

This series of InAsP/InP CS NWs indicate that by systematically increasing As content in the InAsP core, phase mixing can be suppressed completely. In this series for As/P ratio of 0.50 NWs with fewer stacking faults are obtained whereas further increase in the As/P ratio give stacking faults free NWs. This suppression of stacking faults is demonstrated by μ – PL analysis carried out for each of the sample and several NWs from each sample are studied. The NWs rich in stacking faults (Fig. 1a) show a broad μ – PL spectra showing large degree of inhomogeneity, while NWs grown with As/P ration of 0.60 exhibit greater degree of homogeneity (Fig. 1b) with a considerable decrease in the width of PL peak. This strongly suggest that increasing As content modifies the crystal structure and yields defect free NWs. Red shift in the emission energy with increasing As content indicate the higher As incorporation in the InAsP core whereas the decrease in the FWHM is the evidence of the good crystal quality of these NWs.

A red shift for the emission related to InP shell is observed Fig. 3(a). There are two possible explanations for the red shift in the emission energy related to InP, with increasing As content. Firstly, it could be due to the two formation of InAsP shell with parasitic As present in the chamber at the time of the shell growth. Short growth time and low growth temperature for shell enhance As incorporation. The trend of this red shift fit well with increasing As content in the core which implies increased amount of residual As in the chamber at the time of shell growth for respective sample. Secondly, this shift could be related to the stain present in the InP shell around InAsP core and increased As in the core result increasing strain in InP shell. Since the diameter of the inner core is ~10 nm and the shell around these NWs is 15 – 20 nm thick, such red shift only due to strain is not envisioned.

In Fig. 5, band gap energy for ZB $InAs_{1-x}P_x$ ternary is plotted in black for x between 0 and 1 [11]. Peak PL emission energies corresponding to InP shell plotted in Fig. 3 are inserted. Band gap 1.49 eV is considered for the WZ InP (Jancu, 2010), (Pemasiri, 2009). InP emission from sample with As/P ratio of 0.60 which exhibits peak at 1.43eV is inserted with 60 meV difference from the WZ InP and it results with ~ 5% content in the shell. This value, for the parasitic incorporation of As, is quite high so strain should have some effect for this sample. For the samples grown with lower As/P ratio the shift in the emission peak with respect to the WZ InP gives around 2% As incorporation in the shell.

An increasing As incorporation trend is observed and the PL emission give 11%, 13% and 21% incorporation of As in the ternary core for the samples grown with 0.38, 0.50 and 0.60 As/P ratio respectively. For the sample grown with 0.50 As/P ratio nominal As in the core measured by EDS is around 8%. So this additional shift could also be related to the strain.

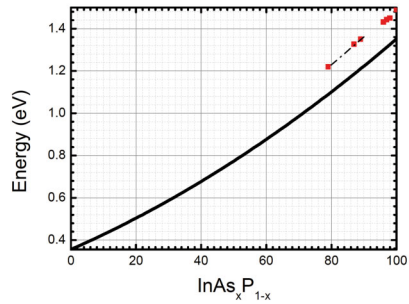

Fig. 5 > µBand gap energy of ternary $InAs_xP_{1-x}$ compound plotted against x ranging between 0 and 1. Red dots with a shift close to difference of ZB and WZ InP band gap energy representing the emission for shell above 1.42 eV and corresponds to core emission between 1.38 eV and 1.22 eV.

Conclusion

In conclusion we have reported the growth of stacking fault free InAsP/InP CS NWs confirmed by their µ – PL analysis. Increase in *As* content in the core part results in suppression crystal imperfection and a blue shift in PL emission energy related to the core emission indicate a systematically increasing *As* content in the core part.

References

[1] N. Akopian. Et al, Nano Lett., 10. 1198 (2010).
[2] E. D. Minot, et al, Nano Lett., 7. 367 (2007).
[3] M. Tchernecheva et al., Nano Lett. 7 (2007) 1500.
[4] F. Jabeen et al., Appl. Phys. Lett. 93 (2008) 083117.
[5] G. Wuet al., Chem. Phys. Lett., 378 (2003) 368.
[6] F. Jabeen et al., to be published, (2011).
[7] J.-M. Jancu et al., Appl. Phys. Lett. 97 (2010) 041910.
[8] K. Pemasiri et al., Nano Lett. 9 (2) (2009) 648.
[9] J. Bao et al., Nano Lett. 8 (3) (2008) 836.
[10] L. V. Titova et al., Nano LettL 7 (11), (2007) 3383.
[11] Brigham Young University (BYU), "Energy gap in III-V ternary semiconductors", http://www.cleanroom.byu.edu/EW_ternary.phtml. ✱

nanojobs

• **Master + PhD Position (CEA, Leti, Grenoble, France):** *"Development of XRR and GIXRF combined analysis"*

The micro and nano electronic world is experiencing a revolution in order to tackle challenges of miniaturization, power consumption, power density and processing speed of CMOS devices. There is now a critical need for metrology to give quantitative chemical composition measurement of new materials with buried interfaces and with nanometre depth resolution.

The deadline for submitting applications is January 14, 2012

For further information about the position, please contact:

Emmanuel Nolot (emmanuel.nolot@cea.fr)

• **PhD or PostDoctoral Position (RWTH Aachen University, Germany):** *"Semiclassical Simulation of CNT- and Graphene FETs"*

The deadline for submitting applications is January 15, 2012

For further information about the position, please contact:

Christoph Jungemann (christoph.jungemann@ithe.rwth-aachen.de)

• **Master + PhD Position (CEA Grenoble, INAC, SPSMS, LaTEQS, France):** *"Non-adiabatic silicon electron pumps"*

An experimental investigation of a new kind of electron pumps is proposed. Electron pumps are two-terminal devices transferring electrons one by one, hence producing a quantized current I=ef for a driving frequency f. These devices are at the heart of a future redefinition of the S.I. unit for electrical current, the ampère, which would, like other units, be related to fundamental constants (here the charge e of an electron).

The deadline for submitting applications is January 18, 2012

For further information about the position, please contact:

Xavier Jehl (xavier.jehl@cea.fr)

nanoconfs

• **Architecture & Design of Molecule Logic Gates and Atom Circuits (AtMol conference series)**

January 12-13, 2012. Barcelona (Spain)

http://atmol.phantomsnet.net/Barcelona2012_index.php?project=7

Atomic Scale Technology

• **Nanospain2012**

February 27 - March 01, 2012. Santander (Spain)

www.nanospainconf.org/2012/

NanoBiotechnology, NanoChemistry, Nanotechnologies

• **nanotech 2012**

February 15-17, 2012. Tokyo (Japan)

www.nanotechexpo.jp/en/

Nanotechnologies, Nanotechnology Business

• **Bionanotechnology III: from biomolecular assembly to applications**

04-06 January 2012. Robinson College, Cambridge (UK)

www.biochemistry.org/tabid/379/MeetingNo/SA121/view/Conference/default.aspx

Nanomaterials, Nanobiotechnology

• **BioNanoMed 2012: Nanotechnology in Medicine & Biology**

March 01-02, 2012 ,Austria (Spain)

www.bionanomed.at/

Nanobiotechnology, Nanomedicine

nanoresearch

Brillouin light scattering measurements in crystallographically tuned thin Co-films

O. Idigoras[1], B. Obry[2], B. Hillebrands[2] and A. Berger[1]

[1] CIC nanoGUNE Consolider, Tolosa Hiribidea 76, E-20018 Donostia-San Sebastian, Spain.
[2] Fachbereich Physik and Landesforschungzentrum OPTIMAS, Technische Universität Kaiserslautern, Erwin-Schrödinger-Straße 56, D-67663 Kaiserslautern, Germany.

We report an experimental study of spin waves in thin Co-films with in-plane uniaxial symmetry, which were measured by means of the Brillouin light scattering (BLS) technique. In particular, we investigated the effect of the previously discovered hard axis (HA) anomalous magnetization state that occurs during magnetization reversal in partially disordered films. This work has been performed in Prof. Dr. Burkard Hillebrands' group where all members of team were really nice in supporting all the activities. Furthermore, all have been possible thanks to Phantoms Foundation's Nano-ICT project launches exchange visit fellowship.

Introduction

In previous work we have demonstrated that is possible to tune the degree of crystallographic order in Co-films by partial interruption of epitaxy in a well-defined and reproducible manner [1]. Hereby, we utilized an optimized growth sequence to achieve good epitaxy and a high degree of crystallographic order as a starting point. Specifically, we produced epitaxial Co-films with an in-plane hcp c-axis by growing the sequence Ag 75 nm/Cr 50 nm/Co 30 nm/ SiO_2 10 nm onto hydrofluoric etched Si (110) substrates. For the tunable disturbance of the growth sequence, we introduced an ultrathin Si-oxide layer of defined thickness in the order of a single monolayer on top of the Si-substrate prior to the Ag-film growth. By depositing different amounts of Si-oxide, we have obtained a set of samples with different degree of crystallographic order. Moreover, we observe an anomalous magnetic reversal near the HA in these samples above a threshold level of crystallographic disorder, while behavior in all other field orientations is barely affected. This anomaly arises from a competition of the misalignment anisotropy axes with the exchange energy and it gives rise to an unusually high remanent magnetization and coercive field along the hard axis [1].

The Brillouin light scattering (BLS) technique [2] is a powerful method to analyze spin waves and related magnetic properties. Primarily, it allows for the analysis of spin waves energies by means of the frequency shift of inelastically scattered photons from a magnetic sample. Photons interact hereby with spin waves, so that a spin wave is created (Stokes process) and the photon looses energy correspondingly or a spin wave is annihilated (anti-Stokes process) whereupon the photon gains that energy. Experimentally, the frequency shift of the scattered light is detected to measure the corresponding spin wave energy. In this work we have analyzed Stokes scattering processes only.

In general, different spin wave modes can be present in a thin film [3]. The main distinction arises from the type of interaction that dominates them, which is either the exchange or the dipolar interaction. There exist different dipolar dominated modes, which can be bulk or surface spin wave modes. The surface mode, called as magnetostatic surface mode (MSSM) or Damon-Eshbach (DE) mode are excited when the magnetization M and the wave vector lie both in the film plane and are perpendicular to each other. Even in this case

when the magnetization and wave vector are perpendicular bulk modes can be excited, in thin films it is not possible to distinguish between both modes and only MSSM/DE mode are considered. On the other hand, if both are in-plane and parallel, magnetostatic backward volume modes (MSBVM) are excited. For the same in-plane wave vector the DE/MSSM mode has higher energy and thus frequency than the MSBVM mode. The exchange type perpendicular standing spin waves (PSSW) are formed by a superposition of two spin waves that are propagating in opposite directions perpendicular to the film surface. In this work we have analyzed all three spin wave modes, DE/MSSM, MSBVM and PSSW.

The experimental setup that was utilized in this study is equipped with a tandem Fabry-Pérot interferometer [4]. Moreover, this setup is able to perform an automated in-plane rotation of the sample. In this work, we used backward scattering geometry, and all measurements have been done with an in-plane applied field orientation perpendicular to the wave vector.

Influence of the HA anomaly on spin waves spectra

In order to analyze the effect that the HA anomaly has on the spin wave spectra we have measured the dependence of the spin wave frequencies as a function of the applied field strength for (i) an epitaxial sample, in which the anomaly is not present, and (ii) in a sample with a 0.132 nm thick Si-oxide underlayer, for which the anomaly does occur. One example of such spin wave spectra for the epitaxial sample is presented in figure 1. Apart from the elastically scattered light peak at zero frequency, three peaks are clearly visible that correspond to inelastically scattered light from three spin wave modes. While the position of these peaks gives the frequency of the spin wave, the widths of the peaks contain information about the spin wave damping and thus on the magnetization homogeneity. The peak at -27 GHz corresponds to the dipolar spin wave mode (MSSW/DE), while the other two peaks corresponds to exchange spin wave modes (PSSW). Measurements as the one shown in figure 1 but for multiple applied field strengths are shown in figure 2 as a color map. Figure 2(a) shows the data collected when the external field is applied along the EA, and fig. 2(b) when the field is along the HA. The red color indicates the maximum intensity, i.e. the spin wave positions, while the blue color indicates the minimum intensity, i.e. noise level. In both figures two spin wave modes appear, one belonging to the MSSW/DE at lower absolute values of frequency and one representing the PSSW at higher absolute frequency values. As expected in the EA (fig. 2(a)), both spin wave frequency vs. field curves have the same type of behavior. When the field is applied along the HA (fig. 2(b)), however, the dipolar type spin wave shows a more pronounced frequency shift for small applied field than the PSSW mode. The origin of this frequency shift is the in-plane rotation of the magnetization into the direction of the anisotropy axis as the field strength decreases, causing the spin wave to change its character from the DE mode to MSBV mode, which has a lower frequency than the DE mode. This frequency shift for fields applied along the HA has been previously reported in several works [5].

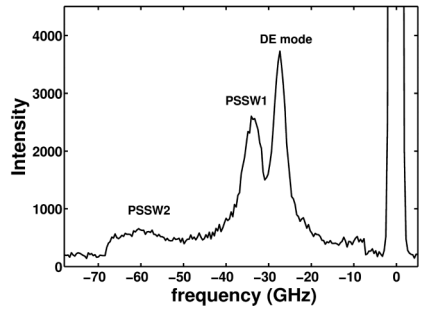

Fig. 1 > Spin wave spectrum for an epitaxial Co (1010)-film sample.

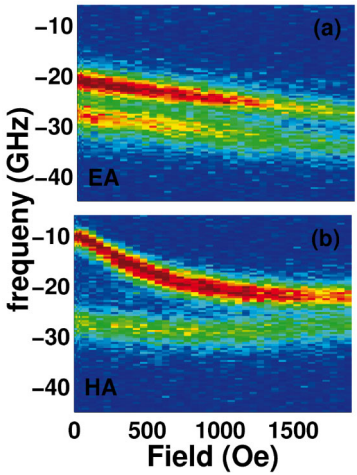

Fig. 2 > (a) and (b) show the spin wave frequency dependence from an externally applied field along the EA and HA, respectively, for an epitaxial Co (1010)-film sample .

A similar set of measurements for a sample, in which the HA anomaly is present (the sample with Si-oxide underlayer of 0.132 nm thickness), are shown in figure 3. Specifically, this figure shows spin wave frequency vs. field dependence for the applied field along the EA (fig. 3(a)), along the HA (fig. 3(b)), and for a field direction 2° away from the HA (fig. 3(c)). Although the dipolar and the exchange type spin waves are close in frequency for measurements along the EA, so that it is difficult to clearly see their separation, both spin waves visibly follow the same frequency behavior as a function of the applied field, just as in the case of epitaxial sample. However, the expected downward frequency shift for the dipolar type spin wave upon reducing the externally applied field along the HA does not occur here (fig. 3(b)). Only a broadening is observed that can arise due to an inhomogeneous sample magnetization. Such an inhomogeneous magnetization state was indeed observed earlier on the same sample by means of Kerr effect microscopy in a narrow range of field orientations around the nominal hard axis [1].

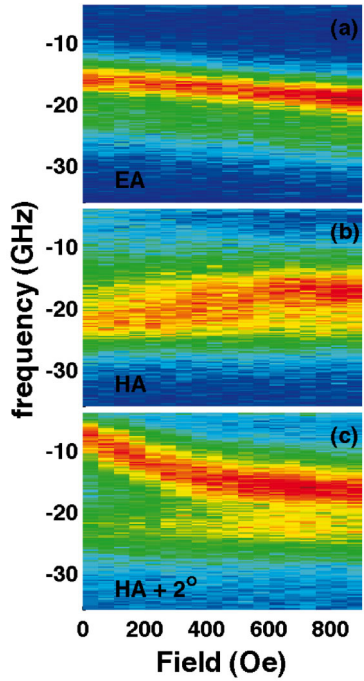

Fig. 3 > (a), (b) and (c) show the spin wave frequency dependence from an externally applied field along the EA, HA and 2° away from the HA, respectively for a uniaxial, but slightly disordered sample.

If the field is applied 2° away from the HA, a conventional HA spin wave behavior reemerges, with the dipolar type spin wave frequency shifting towards lower frequencies upon decreasing the applied field strength. For this sample, the saturation magnetization is obtained at smaller external field strengths than in the case of the epitaxial sample, so that the position shift of this mode is limited to a narrower applied field range.

For the same sample, we have also performed applied field angle β dependent measurements in the vicinity of the HA (β=90°) in remanence. Figure 4(a) shows

spin wave spectra vs. β in remanence after saturating the sample in 1500 Oe for each angle and figure 4(b) shows at the same type of measurment in remanence, but after saturating the sample only once along the EA. In the first measurement (fig. 4(a)) one can see that due to the anomalous magnetization reversal in the HA, β=90°, the dipolar type spin wave is shifted towards higher frequencies. One can also see that a misalignment of only ±1° away from the HA already causes an almost complete suppression of this anomalous behavior and the reappearance of the typical dipolar spin wave at low frequencies of about 7 GHz. In the second measurement series of the same sample after a single EA saturarion (fig. 4(b)), no anomaly is visible, as expected because in this case we only measure the EA projections of the same uniform magnetization state along the applied field direction.

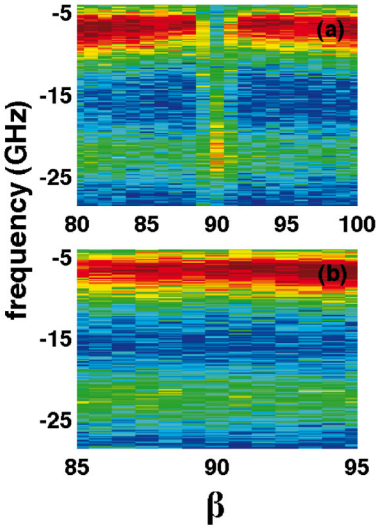

Fig. 4 > Spin wave frequency as a function of the applied angle in remanence for a slightly disordered sample, after (a) prior saturation at every angle and (b) after prior saturation along the EA.

I acknowledges Phantoms Foundation for Nano-ICT project launches exchange visit fellowship, as well as, all members of Prof. Dr. Burkard Hillebrands' group at Fachbereich Physik at Technische Universität of Kaiserslautern and specially Prof. Dr. Burkard Hillebrands for giving me the opportunity to work in his group and Björn Obry with whom I have performed all the measurements and helps me with everything. I also thank the Basque Government for fellowships No. BFI09.284.

References

[1] O. Idigoras, A.K. Suszka, P. Vavassori, P. Landeros, J.M. Porro and A. Berger, submitted to Phys. Rev. B.

[2] O. Gaier, 2009. A study of exchange interaction, magnetic anisotropies, and ion beam induced effects in thin films on Co2-based Heusler compounds. Thesis, (PhD). Technischen Universität Kaiserslautern.

[3] B. Hillebrands, Brillouin light scattering from layered magnetic structures, in M. Cardona, Güntherodt (Editors), Light Scattering in Solids VII, vol. 75 of Topics in Applied Physics, Springer Verlag, Berlin Heidelberg (2000).

[4] J.R. Sandercock, Opt. Comm. 2, 73 (1970). B. Hillebrands, Rev. Scien. Instr. 70, 1589 (1999).

[5] R. Scheurer, R. Allenspach, P. Xhonneux and E. Courtens, Phys. Rev. B 48, 9890 (1993). M. Grimsditch, E.E. Fullerton and R.L. Stamps, Phys. Rev. B 56, 2617 (1997). ✱

nanoresearch

Temperature distribution of heated membranes for stencil lithography application

Shenqi Xie[a], Damien Ducatteau[b], Bernard Legrand[b], Veronica Savu[a], Lionel Buchaillot[b] and Juergen Brugger[a]

[a] Microsystems Laboratory (LMIS-1), Ecole Polytechnique Fédérale de Lausanne, Switzerland.
[b] Institut d'Electronique, de Microélectronique et de Nanotechnologie, UMR CNRS 8520, IEMN, Avenue Poincaré, B.P. 69, 59652 Villeneuve d'Ascq Cedex, France.

1. Introduction

Stencil lithography (SL) is a resistless lithography method for surface patterning with sub-micron resolution. As the most conventional application of SL, thin-film deposition has become a reliable micro/nano-patterning process [1, 2]. However, the useful life time of the stencil during one pump-down is limited by the clogging of the aperture due to the deposited material [3]. We recently developed a novel approach to potentially prevent and eventually eliminate clogging by locally heating up the stencil during metal deposition, minimizing thus materials' condensation on the membrane [4]. The heatable stencil has Pt microhotplates embedded in two layers of SiN thin film, with stencil apertures in between the coils, as shown in figure 1.

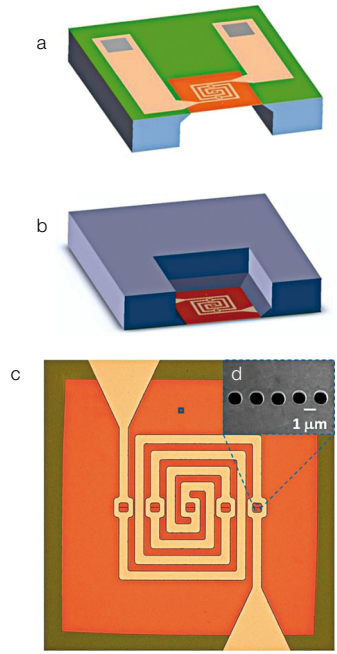

Fig. 1 > Schematics of (a) frontside and (b) backside of the heated stencils. (c) Optical image of the device and (d) SEM image of the apertures in between the coils.

In our previous experiments, the thickness of condensed metal film is correlated to the temperature distribution on the membrane. The area with least material condensation is in the center of the heated membrane, where has the highest temperature. As temperature drops rapidly from the center to the border of the membrane, metal starts accumulating very quickly during deposition, which of course increases clogging rate. Therefore, it is critical to know the precise temperature distribution on the membrane in order to study the relation between temperature and condensation rate, which can be translated into clogging rate. In addition, the temperature coefficient of resistance (TCR) can be extracted from the temperature mapping under certain input power in ambient conditions. As the heated stencil will be placed in the vacuum chamber of an E-beam evaporator, the temperature of the membrane can only be calculated from the variation of the resistance of the microhotplate based on the measured TCR in order to monitor the process. By using the

high resolution (3 µm) InSb IR microscope in IEMN, we are able to measure the precise temperature in the area close to the stencil apertures, which provides us the feasibility of studying the dependence of temperature on clogging rate.

2. Infrared measurement

The microhotplate was powered below the IR microscope for recording thermal images. Various designs of the coils with different resistance were measured. Figure 2(a) shows the thermal image of one of the designs taken under 1.0 V bias. The highest temperature appears in the centre of the microhotplate, which agrees well with the results from simulation. Several measurements were performed under different input power, and the temperature extracted from each image was used to calculate the TCR. Since the TCR for thin Pt film is different from its bulk form, this calibration is necessary. Figure 2(b) shows the measured temperature with corresponding resistance. Due to the limitation of the detection range, the highest measurable temperature is around 430 °C. The TCR acquired from the linear fit is 1.947e-3/K. This calculated value will be used to monitor the temperature during metal deposition in vacuum.

Further analysis of the thermal image provides us the temperature profile of the membrane, which is not smooth as shown in the black curve in figure 3(a). The temperature on the SiN area in between the Pt coils drops dramatically. In fact, it is due to the difference of emissivity on different materials. Therefore, SiN looks more transparent than Pt in the infrared range, which gives us a much lower temperature. In order to have a more accurate thermal mapping, thin layers of Pt were coated on the frontside of the membrane, offering a more uniform surface in terms of emissivity. Measurements were done under the same conditions before and after Pt coating, as shown in figure 3(a). The temperature profile becomes much smoother after Pt coating.

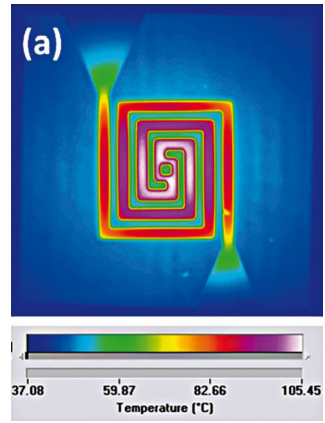

Fig. 2 > (a) Thermal image of one of the coil designs powered under 1.0 V bias. (b) The measured temperature with corresponding resistance. The TCR extracted from the curve is 1.947e-3/K.

However, the drawback is that the coated Pt thin film increases the thermal conductivity on the membrane. Thus, more heat was dissipated from the membrane, which of course decreases the average temperature. But still, it offers us the possibility of estimating the temperature around the stencil apertures within an acceptable error. In addition, due to the spiral layout of the electrode, a stronger thermal coupling effect must happen in the middle of the membrane, which decreases the temperature gradient in that area. The

relatively uniform temperature distribution in the centre of the membrane provides a stable thermal environment for the stencil apertures.

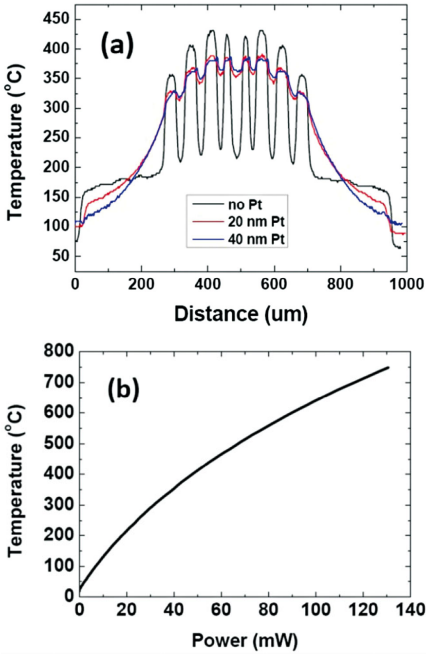

Fig. 3 > (a) The temperature profile of the heated stencil with and without Pt coating on the frontside of the membrane. (b) The average temperature of the membrane versus the applied power in ambient conditions.

Another information can be derived from the measurement is the temperature versus power consumption, as shown in figure 3(b). The power consumption is not critical in our preliminary stage of experiments, but it has to be considered in future development if more heated stencils are powered simultaneously.

3. Conclusions

We have successfully carried out the thermal measurement on heated stencils by using the IR microscope in IEMN. Various designs of the coils with different resistance were measured, which provides important information for optimizing the designs in future generations. The calibrated temperature coefficient of resistance (TCR) is extremely useful in monitoring and controlling the whole process. Temperature profiles were also studied to correlate with the clogging rate in different areas. Extra Pt thin layers were coated on the membrane for providing a more uniform surface in terms of emissivity, leading to a more accurate temperature measurement. The temperature distribution provides us great feasibility of studying the dependence of temperature on clogging rate. The achieved results from this exchange program would be combined with other results to be considered to submit to MEMS2012, following with other journals.

References

[1] M. A. F. van den Boogaart, et al., "Corrugated membranes for improved pattern definition with micro/nanostencil lithography", Sensors and Actuators A, vol. 130-131, p. 568-574, 2006.

[2] V. Savu, et al., "Dynamic stencil lithography on full wafer scale", Journal of Vacuum Science and Technology B, 26(6), 2008.

[3] M. Lishchynska, et al., "Predicting Mask Distortion, Clogging and Pattern Transfer for Stencil Lithography", Microelectronic Engineering, 84 (2007) 42-53.

[4] S. Xie, V. Savu, J. Brugger, "Heated membranes prevent clogging of apertures in nanostencil lithography", The 16th International Conference on Solid-State Sensors, Actuators and Microsystems (Transducers'11), Beijing, China. *

graphene 2012

April 10-13, 2012
Brussels (Belgium)
www.graphene2012.com

graphene
International Conference

Graphene Flagship Session

The consortium of the Graphene Flagship Pilot Action is working to establish the "Graphene Science and Technology Roadmap" which will be presented to the European Commission and Member States to demonstrate the need for securing long term funding, coordinated through a new Graphene Alliance. The Graphene Flagship Pilot Action will take advantage of the International conference Graphene2012 in Brussels to co-organize a specific session in order to timely deliver to the European community the results of this Roadmap.

PHANTOMS foundation

UCL Université catholique de Louvain

ICN Institut Català de Nanotecnologia

cnrs